

Photometric transit search for planets around cool stars from the western Italian Alps: A pilot study

P. Giacobbe¹, M. Damasso^{2,3}, A. Sozzetti^{4*}, G. Toso², M. Perdoncin⁵, P. Calcidese², A. Bernagozzi², E. Bertolini², M. G. Lattanzi⁴, and R. L. Smart⁴

¹*Dept. of Physics, University of Trieste, Via Tiepolo 11, I-34143 Trieste, Italy*

²*Astronomical Observatory of the Autonomous Region of the Aosta Valley, Loc. Lignan 39, 11020 Nus (Aosta), Italy*

³*Dept. of Astronomy, University of Padova, Vicolo dell'Osservatorio 3, I-35122 Padova, Italy*

⁴*INAF - Osservatorio Astronomico di Torino, Via Osservatorio 20, I-10025 Pino Torinese, Italy*

⁵*Dept. of Physics, University of Torino, Via Giuria 1, I-10125 Torino, Italy*

Accepted ???. Received ???

ABSTRACT

We present the results of a year-long photometric monitoring campaign of a sample of 23 nearby ($d < 60$ pc), bright ($J < 12$) dM stars carried out at the Astronomical Observatory of the Autonomous Region of the Aosta Valley, in the western Italian Alps. This program represents the ‘pilot study’ for a long-term photometric transit search for planets around a large sample of nearby M dwarfs, due to start with an array of identical 40-cm class telescopes by the Spring of 2012. In this study, we set out to *a*) demonstrate the sensitivity to $< 4 R_{\oplus}$ transiting planets with periods of a few days around our program stars, through a two-fold approach that combines a characterization of the statistical noise properties of our photometry with the determination of transit detection probabilities via simulations, and *b*) where possible, improve our knowledge of some astrophysical properties (e.g., activity, rotation) of our targets by combining spectroscopic information and our differential photometric measurements. We achieve a typical nightly RMS photometric precision of ~ 5 mmag, with little or no dependence on the instrumentation used or on the details of the adopted methods for differential photometry. The presence of correlated (red) noise in our data degrades the precision by a factor ~ 1.3 with respect to a pure white noise regime. Based on a detailed stellar variability analysis, *a*) we detected no transit-like events (an expected result given the sample size); *b*) we determined photometric rotation periods of ~ 0.47 days and ~ 0.22 days for LHS 3445 and GJ 1167A, respectively; *c*) these values agree with the large projected rotational velocities (~ 25 km/s and ~ 33 km/s, respectively) inferred for both stars based on the analysis of archival spectra; *d*) the estimated inclinations of the stellar rotation axes for LHS 3445 and GJ 1167A are consistent with those derived using a simple spot model; *e*) short-term, low-amplitude flaring events were recorded for LHS 3445 and LHS 2686. Finally, based on simulations of transit signals of given period and amplitude injected in the actual (nightly reduced) photometric data for our sample, we derive a relationship between transit detection probability and phase coverage. We find that, using the BLS search algorithm, even when phase coverage approaches 100%, there is a limit to the detection probability of $\approx 90\%$. Around program stars with phase coverage $> 50\%$ we would have had $> 80\%$ chances of detecting planets with $P < 1$ day inducing fractional transit depths $> 0.5\%$, corresponding to minimum detectable radii in the range $\sim 1.0 - 2.2 R_{\oplus}$. These findings are illustrative of our high readiness level ahead of the main survey start.

Key words: planetary systems – stars: low-mass – stars: activity – stars: spots – stars: individual: GJ 1167A, LHS 2686, LHS 3445 – techniques: photometric

1 INTRODUCTION

M dwarf stars, with masses $M_{\star} \leq 0.6 M_{\odot}$, make up the vast majority of the reservoir of nearby stars within $\sim 25 - 30$ pc. These stars have not traditionally been included in large numbers in the target

* E-mail: sozzetti@oato.inaf.it

lists of radial-velocity (RV) searches for planets for two main reasons: 1) their intrinsic faintness, which prevented Doppler surveys in the optical from achieving very high radial-velocity precision ($< 5 - 10$ m/s) for large samples of M dwarfs (e.g., Eggenberger & Udry 2010, and references therein), and 2) their being considered as providers of very inhospitable environments for potentially habitable planets (e.g., Tarter et al. 2007; Scalo et al. 2007, and references therein). These two paradigms are now shifting. First, the application of the transit technique to M dwarfs presents several exciting opportunities, and the advantages are especially compelling for the detection of transiting habitable, rocky planets. These include, for example, improved observing windows due to the short periods of potential planets in the stellar habitable zone (the range of distances from a given star for which water could be found in liquid form on a planetary surface. E.g., Kasting et al. 1993), or the possibility to reach detection of rocky planets due to the small radii of M dwarfs, leading to deep transits ($\Delta mag \sim 0.005$ mag) easily detectable from the ground with modest-size telescopes (30–50 cm class), and readily confirmable with present-day precision RV measurements (owing to their moderately large RV amplitudes, on the order of 5–10 m/s). Second, while not all concerns about their habitability have been resolved yet, there has been a recent change in view for planets orbiting low-mass M stars, now often considered as potentially hospitable worlds for life and its remote detection (e.g., Seager & Deming 2010; Barnes et al. 2011, and references therein).

Advancements in our knowledge of the complex processes of planet formation and evolution cannot be achieved without a detailed understanding of the role of the central star (through its properties such as mass and metal abundance) and its environment (the circumstellar disk within which the planetary population must form). For example, the theoretical expectations (within the framework of the standard core accretion model) that giant planet frequency and upper mass limits ought to be direct functions of stellar mass M_* and metallicity [Fe/H] (e.g., Laughlin et al. 2004; Ida & Lin 2004, 2005; Kennedy & Kenyon 2008; Mordasini et al. 2009) have so far been confirmed on relatively firm statistical grounds only for stars (mid-F through mid-K type) with masses close to that of the Sun (Santos et al. 2004; Fischer & Valenti 2005; Johnson et al. 2007; Sozzetti et al. 2009), while results for stars with masses significantly different from that of the Sun still rely on small-number statistics (e.g., Endl et al. 2006; Bonfils et al. 2007; Johnson et al. 2010, 2011, 2012). Similarly, the statistical significance of the early evidence for a relatively high frequency of low-mass planets (Neptunes and super-Earths) around low-mass stars (e.g., Forveille et al. 2011, and references therein) is still hampered by the observational bias intrinsic to long-term RV surveys (only a few hundred objects monitored), and the recent, compelling evidence from Kepler photometry (e.g., Howard et al. 2011) of increasing occurrence rates for small-radius, short-period planets around increasingly cooler stars still suffers from small-numbers statistics at the latest spectral types (only a few hundred of relatively bright M0–M1 dwarfs being included in the Kepler catalogue). Finally, the anticipated wild diversity of the structural and atmospheric properties of super-Earths (Seager & Deming 2010, and references therein) can be most easily investigated using a sample of such planets observed as transiting companions to nearby M dwarf primaries, given that for low-mass stars the planet-to-star flux ratio is much larger than that for the Earth-Sun system¹, thus spectral characterization of

the planet via, e.g., occultation spectroscopy is much more readily attainable.

These considerations have brought about renewed efforts to monitor photometrically as well as spectroscopically large samples of nearby cool dwarfs. The first spectacular success of the dedicated MEarth transit search for rocky planets around 2000 late M dwarfs was announced by Charbonneau et al. (2009), with the detection of the low-density transiting super-Earth GJ 1214b ($M_p = 6.5 M_\oplus$, $R_p = 2.7 R_\oplus$) around a nearby M4.5 dwarf. The primary in this system is bright enough to enable the detailed spectroscopic characterization of the planet’s thick atmosphere over a broad wavelength range (Bean et al. 2010, 2011; Croll et al. 2011; Crossfield et al. 2011). The recent constraints on GJ 1214b’s atmospheric composition are not only essential for breaking the degeneracy between the mass, radius and composition of both the interior and a possible atmosphere in theoretical models of super-Earths (Adams et al. 2008; Rogers & Seager 2010; Miller-Ricci & Fortney 2010; Miller-Ricci et al. 2011; Désert et al. 2011; Nettelmann et al. 2011; Menou 2011), but they also constitute a remarkable test of planetary evolution models in a mass range (for both the primary and the planet!) not seen in our Solar System. Very recently, the M2K Doppler search for close-in planets around 1600 nearby M and K dwarfs has also started producing its first results (e.g., Apps et al. 2010). Decade-long Doppler monitoring has also allowed to detect the first Saturn-mass planet in the habitable zone of a nearby mid-M dwarf (Haghighipour et al. 2010). The early-M dwarf GJ 581, already hosting a system of four low-mass (Neptunes and super-Earths) planets, is currently the focus of a hot debate on the actual existence of a fifth planet with the mass of a super-Earth orbiting right in the middle of the habitable zone (Vogt et al. 2010; Tuomi 2011; Pepe et al. 2011; Gregory 2011). There is a growing consensus among the astronomers’ community that the first habitable rocky planet will be discovered (and might have been discovered already!) around a red M dwarf in the backyard of our Solar System.

However, not all physical properties of low-mass stars are known precisely enough for the purpose of the detection and characterization of small-radius planets. Worse still, some of the characteristics intrinsic to late-type dwarfs can constitute a significant source of confusion in the interpretation in planet detection and characterization measurements across a range of techniques. First of all, there exist discrepancies between theory and observations in the determination of the sizes of M dwarfs, typically on the order of 10%-15% (Ribas 2006; Beatty et al. 2007; Charbonneau et al. 2009, and references therein). It has been suggested that this problems might be stemming from the lack of a detailed treatment of the effects of non-zero magnetic fields on the properties of low-mass, fully convective stars (Ribas 2006; López-Morales 2007; Torres et al. 2010, and references therein). As a result, the inferred composition of a transiting planet detected around an M dwarf might be subject to rather large uncertainties, particularly when it comes to super-Earths, for which, as mentioned above, degeneracies in the models of their physical structure indicate a wide range of possible compositions for similar masses and radii (Seager & Deming 2010, and references therein). Indeed, for the two known transiting planets around M dwarfs, GJ 436b and GJ 1214b, uncertainties in the

relative surface areas and brightness temperatures of the planet and star. For a $2-M_\oplus$ super-Earth, this ratio is in the range 0.01%-0.11% for a mid- to late-M dwarf primary (M4V–M8V), compared to 0.00044% for the Earth-Sun system.

¹ For example, in the Rayleigh-Jeans limit, this flux ratio depends on the

planetary parameters are dominated by the limits in the knowledge of the stellar parameters.

Second, there are at present difficulties in spectroscopically determining with a high degree of precision M dwarf metallicities² (Bean et al. 2006; Woolf & Wallerstein 2006; Woolf et al. 2009; Rojas-Ayala et al. 2010), which are only partially mitigated by recent attempts at deriving photometric calibrations (Bonfils et al. 2005; Casagrande et al. 2008; Johnson & Apps 2009; Schlafman & Laughlin 2010). In addition, studies of the rotation-activity relation³ for M dwarfs using large stellar samples are limited to young and active stellar samples (e.g., Shkolnik et al. 2009; López-Santiago et al. 2010, and references therein), often in young open clusters (e.g., Meibom et al. 2009; Hartman et al. 2009, and references therein), while our understanding of the rotation-activity connection for M dwarfs with age greater than $t \sim 0.5$ Gyr (e.g., Pizzolato et al. 2003; Reiners 2007; Jenkins et al. 2009; West & Basri 2009) is still subject to rather large uncertainties due to the sparseness of the data. All these issues hamper at present the possibility of determining precisely the ages of (particularly mid- and late-) M dwarfs in the field, and this in turn has a significant impact on the calibration of the fundamental evolutionary properties of the planets they might be hosting.

Third, as measurements of chromospheric activity indicators (H α line) have shown how the fraction of active M dwarfs increases as a function of spectral sub-type (e.g., Bochanski et al. 2005; West et al. 2011), activity-related phenomena such as stellar spots, plages, and flares become increasingly a matter of concern for planet detection and characterization programs targeting late-type stars. Stellar surface inhomogeneities can hamper the detection, and sometimes even mimic the signal, of exoplanets (e.g., Queloz et al. 2001), and seriously complicate the characterization of their properties. This problem has already become acute in the case of active solar analogs hosting transiting planets. An illustrative example is provided by the ongoing debate on the actual mass of CoRoT-7b, varying (including 1- σ uncertainties as large as 20%) between 1 M_{\oplus} and 9 M_{\oplus} (!), depending on how one decides to deal with the modelling of the planetary signal superposed to the much larger activity-induced stellar ‘jitter’ in both the photometric and the radial-velocity measurements (Queloz et al. 2009; Hatzes et al. 2010; Pont et al. 2011; Ferraz-Mello et al. 2011). Recently, the first serious studies attempting to gauge the limits to planet detection induced by stellar activity-related phenomena, and strategies aiming at minimizing such effects, have been undertaken. These have focused primarily on the impact of, and possibility of calibrating out, activity-induced jitter in high-precision radial-velocity and astrometric measurements (Makarov et al. 2009; Lagrange et al. 2010; Boisse et al. 2011, and references therein; Dumusque et

al. 2011; Sozzetti 2011, and references therein). Very recently, the first analyses of the impact of starspots on radial-velocity searches for earth-mass planets in orbit about M dwarf stars have been carried out by Reiners et al. (2010) and Barnes et al. (2011), who also addressed the merit of moving from the optical to infrared wavelengths (where the starspots-induced RV noise might be significantly reduced).

All the above considerations clearly underline how achieving the goal of the detection *and* characterization of low-mass, potentially habitable, rocky planets around low-mass stars requires the construction of a large (all-sky) sample of nearby, relatively bright M dwarfs with well-characterized properties. This will necessitate the combined use of time-series of spectroscopic, astrometric, and photometric data of high quality. In particular, the jitter levels will have to be quantified in detail for each target individually, as the jitter properties may vary from star to star within the same spectral class, as suggested by recent findings based on high-precision Kepler photometry (e.g., Ciardi et al. 2011) and high-resolution, high-S/N spectroscopy (e.g., Zechmeister et al. 2009). With kick-off in December 2009, we have carried out a year-long pilot study for an upcoming photometric transiting search for small-size planets around thousands of nearby M dwarfs which will utilize an array of five 40-cm telescopes at the Astronomical Observatory of the Autonomous Region of the Aosta Valley (OAVdA), in the western Italian Alps. The OAVdA site was selected on the basis of a detailed site characterization study (Damasso et al. 2010). The pilot study was focused on the medium-term (typically for 2 months) photometric monitoring, using small-size instrumentation (25-80 cm class telescope systems), of a sample of 23 cool M0-M6 dwarfs with good parallaxes from the TORINO Parallax Program (TOPP; Smart et al. 2010). The primary objectives we set out to achieve in this study were *a*) to demonstrate sensitivity to $< 4 R_{\oplus}$ (i.e., smaller than radius of Neptune) transiting planets with periods of a few days around our sample, through a two-fold approach that combines a characterization of the statistical noise properties of our photometry with the determination of transit detection probabilities via simulations, and *b*) where possible, to better our knowledge of some astrophysical properties (e.g., activity, rotation, age) of our targets through a combination of spectroscopic and astrometric information and our differential photometric measurements.

In § 2 we describe the OAVdA instrumentation utilized during the pilot study, and outline the dedicated pipeline for the data processing and analysis of the photometric data we have developed. We discuss in § 3 the main characteristics of the M dwarf sample targeted by the pilot study, and present in § 4 the main results of the study in terms of 1) achieved short-term and medium-term photometric sensitivity for our sample, 2) improved characterization of the properties of the cool M dwarfs observed, by combining the knowledge of their photometric micro-variability time-scales with other available spectroscopic, photometric, and astrometric observations, and 3) a careful assessment of the limits to transiting planetary companions for each star in our sample. We conclude in § 5 by summarizing our findings and by discussing the preparatory steps for the upcoming long-term photometric monitoring program to characterize the micro-variability features of and search for transiting small-size planetary companions to a well-defined sample of low-mass stars, to be carried at the OAVdA site in the near future.

² M-dwarf spectra are dominated by chemically complex molecular features. As a result, the identification of the continuum in an M dwarf spectrum is challenging, rendering line-based metallicity indicators unreliable. The poorly constrained molecular opacity data currently available make the determination of metallicity through spectral synthesis also difficult (e.g., Gustafsson 1989; West et al. 2011, and references therein).

³ The connection between stellar rotation and activity is usually investigated by means of 1) spectroscopic measurements of the rotational velocity $v \sin i$, usually coupled to measurements of the H α luminosity (e.g., Reiners & Basri 2010, and references therein), 2) spectroscopic monitoring of temporal evolution of the R'_{HK} activity index as determined from the Ca II H & K emission line cores (e.g., Wright et al. 2004), and 3) photometric determination of rotation periods for stars with significant spot coverage (e.g., Strassmeier et al. 2000).

2 INSTRUMENTATION AND METHODOLOGY

The instrumental set up used in this study is very similar to the one adopted for the OAVdA site characterization study described in Damasso et al. (2010). In summary, we used a small-size telescope array composed of three instruments with diameters of 81 cm, 40 cm, and 25 cm, respectively. For the purpose of the pilot study described here, the 40-cm and the 25-cm telescopes performed all the observations equipped with standard Johnson-Cousins *I* filters, while the 81-cm utilized a standard Johnson-Cousins *R* filter (observations in the *I* filter with this instrument were affected by fringing). Naturally, the choice of filters was driven by red colours of the target sample. In Table 1 we summarize the main characteristics of the telescope and camera systems.

All observations were performed with the CCDs set up at the focus of the telescope, and the exposure times were chosen at the beginning of each night of observation (without being subsequently modified) in order to guarantee an optimum signal-to-noise ratio ($S/N \gtrsim 100$) for the target, while avoiding saturation (see Table 2 for the typical exposure times for each monitored target). The temporal sampling, including overheads, was typically of a few minutes. We chose to observe with any given instrument one star at a time during a night, tracking it without repointing. No auto-guiding was utilized for the 25cm and 40cm telescopes (as described already in Damasso et al. 2010). For the two instruments, we recorded typical drifts of up to 100 pixels. None of the above elements of the observing strategy was optimized with the intent of reproducing the actual one to be implemented in our upcoming survey, which will employ vastly improved instrumentation and an adaptive observing strategy to be described in a future work. In this respect, the resulting photometric performances reported here can be considered as conservative.

For the pilot study we selected 23 targets from the input target list of the TOPP Program (see § 3 for details). We chose an observational strategy which would allow us to monitor each target for at least 3 hr/night without interruptions for a minimum of a dozen nights over a maximum period of ~ 2 months. The expected phase coverage for transiting companions within a few (1-2) days of period would exceed 70%. Two stars, LHS 1976 and LHS 534, were observed for a significantly longer period of time (LHS 1976 actually over two seasons), in order to probe our sensitivity to transiting companions on periods of up to about 1 week or so. At the end of the pilot study (a little over 1 year of observations) the whole database comprised 76287 good images, corresponding to ~ 1000 GB of data. A summary of the pilot study observations is provided in Table 2.

The data reduction procedure utilizes an upgraded version of TEEPEE (Transiting Exoplanets PipelinE), described in detail in Damasso et al. (2010). In short, TEEPEE is a software package written in IDL⁴, which utilizes publicly available software from the Astronomy Users' Library⁵ as well as external contributed FORTRAN routines. The areas of the software written from scratch by two of us (PG and MD) are the ones devoted to automatically carry out ensemble differential aperture photometry on a user-specified target. TEEPEE is organized in three main, sequential modules:

- image calibration (including dark and bias subtraction, and flat fielding)

- astrometric processing (image alignment) and photometric processing (aperture photometry)
- differential photometry of the target with respect to a chosen set of reference stars

The heart of TEEPEE, for the purpose of this study, is the third block. It performs those operations which are necessary to correct, to a high degree of reliability, for systematic effects which cause the degradation of the precision of the photometric measurements, and it produces photometric light curves for hundreds of stars detected in the field. Our differential photometric method performs as follows. For each frame i , we use as the reference magnitude M_{rif}^i the average magnitude of the n reference stars:

$$M_{rif}^i = \frac{\sum_{k=0}^n M_k^i}{n}. \quad (1)$$

M_{rif}^i is then subtracted to the magnitude of the user-defined target M_{target}^i , obtaining the difference $\Delta M^i = M_{rif}^i - M_{target}^i$. The procedure is iteratively repeated for all the reference stars, using as new references the remaining $n - 1$ stars. This procedure is also iteratively repeated for all detected field stars (based on a $3-\sigma$ above background criterion), using as references the n reference stars chosen for the target.

The second and the third modules have been upgraded with respect to the previous version of the software described in Damasso et al. (2010) in order to improve the differential aperture photometric processing in an automatic way.

In the second module we implemented a multi-aperture photometric processing. We settled on twelve apertures, typically ranging between 2 and 4 times average FWHM (varying slightly depending on the telescope used).

In the third module, we first take care of picking up reference objects on a CCD sub-frame, avoiding the chip edges, affected by vignetting which is not fully corrected for during flat-fielding. Second, we use two efficient methods, based on the Burke et al. (2006) prescription, for choosing the appropriate set of references for the target. The first method (*m1*) selects the subset of reference stars which minimizes the RMS of the differential light curve of the target; the second method (*m2*) selects the subset of references which minimizes the RMS of the differential light curve of each potential reference star. Both methods are then applied to all 12 apertures in order to choose the optimal one, on the basis of a minimum-RMS prescription for the target light curve. Next, we filter out outliers using a $3-\sigma$ clipping criterion, and an additional light curve correction to suppress FWHM-related effects (e.g., Irwin et al. 2007). Finally, we apply the SysRem trend filtering algorithm (Tamuz et al. 2005), to correct for unknown systematic effects in the light curves produced with methods *m1* and *m2*. The two resulting light curves are dubbed as produced with methods *m3* and *m4*, respectively. The whole procedure thus produces a total of four light curves for each target, for each night.

With a similar process, four additional light curves are produced for each target over the whole timespan of the observations, which we dub 'full-period' light curves. A single (the more stable) set of reference stars is chosen over the entire observation window. The only information retained from the nightly procedure is the optimal aperture for each night. In place of SysRem, a different trend filtering algorithm is utilized, TFA (Kovács et al. 2005), which after some experimenting was found to be better suited for the full-period light curve analysis.

⁴ IDL is a commercial programming language and environment by ITT Visual Information Solutions. <http://www.ittvis.com/idl/>

⁵ <http://idlastro.gsfc.nasa.gov/contents.html>

Table 1. Summary of the main characteristics of the telescope and camera systems.

| Optical scheme | Telescope | | CCD camera | | Resulting configuration | |
|----------------------------|---------------|-------------|-----------------------------------|-------------------------------------|----------------------------|-----------------------|
| | Aperture (cm) | Focal ratio | Sensor area (pixel ²) | Pixel area (μ m ²) | FoV (arcmin ²) | Plate scale ("/pixel) |
| Reflector Maksutov | 25 | f/3.80 | 2184 × 1472 | 6.8 × 6.8 | 52.10 × 35.11 | 1.43 (binning 1 × 1) |
| Reflector Ritchey-Chrétien | 40 | f/7.64 | 1024 × 1024 | 24 × 24 | 26.4 × 26.4 | 1.55 (binning 1 × 1) |
| Reflector Ritchey-Chrétien | 81 | f/7.90 | 2048 × 2048 | 15 × 15 | 16.3 × 16.3 | 1 (binning 2 × 2) |

Table 2. Log of observations for the target sample.

| ID | LHS | Number of frames | Number of nights | Epoch range (days) | Telescope (cm) | Typical exposure (sec) |
|----|------|------------------|------------------|--------------------|----------------|------------------------|
| 1 | 1104 | 2049 | 14 | 48 | 40 | 61 |
| 2 | 1475 | 6826 | 20 | 72 | 25 | 34 |
| 3 | 228 | 1084 | 18 | 54 | 40 | 155 |
| 4 | 243 | 774 | 14 | 44 | 40 | 137 |
| 5 | 1976 | 24761 | 108 | 482 | 25/81 | 64/7 |
| 6 | 6158 | 2804 | 10 | 40 | 25 | 28 |
| 7 | 269 | 1629 | 14 | 56 | 40 | 60 |
| 8 | 2220 | 3980 | 16 | 58 | 40 | 23 |
| 9 | 283 | 1696 | 12 | 56 | 25 | 58 |
| 10 | 2472 | 1022 | 8 | 57 | 25 | 75 |
| 11 | 360 | 46 | 1 | 1 | 40 | 120 |
| 12 | ... | 4421 | 15 | 64 | 25 | 21 |
| 13 | 417 | 4693 | 34 | 85 | 25/81 | 10/3 |
| 14 | 3343 | 2122 | 17 | 88 | 25/40 | 60/30 |
| 15 | 3445 | 2835 | 19 | 66 | 25 | 54 |
| 16 | 528 | 1697 | 13 | 40 | 25 | 62 |
| 17 | 534 | 7346 | 44 | 122 | 81 | 8 |
| 18 | 1721 | 3028 | 22 | 61 | 81 | 6 |
| 19 | 370 | 633 | 9 | 33 | 81 | 120 |
| 20 | 306 | 75 | 1 | 1 | 40 | 75 |
| 21 | ... | 1265 | 11 | 59 | 25 | 75 |
| 22 | 2686 | 914 | 10 | 60 | 40 | 75 |
| 23 | 2719 | 587 | 7 | 20 | 40 | 90 |

3 STELLAR SAMPLE

As already mentioned earlier, the *M* dwarfs targeted during the pilot study were selected from the TOPP program input list of nearby ($d < 60$ pc) cool stars. We chose stars spanning a range of spectral sub-types, approximately M0 through M6, and set an *I*-band magnitude limit of $I \lesssim 14$ (thus keeping exposure times typically to within a few minutes). These two criteria allowed us to probe potentially different regimes of intrinsic stellar variability (see § 1), both in terms of amplitude and time-scales.

Most of these objects, with the exception of LHS 228, LHS 306, LHS 360, and LHS 2719, are included in the LSPM-North catalog (Lépine & Shara 2005), with either Hipparcos trigonometric parallaxes or distance moduli estimates indicating they are within 33 pc from the Sun (Lépine 2005). Furthermore, for about half of the sample Smart et al. (2010) have published precision astrometric information, including direct distance estimates. For the purpose of this study, and particularly to derive the results presented in § 4.5, it is important to provide reliable estimate of mass M_* and radius R_* for all our program stars. For the targets presented in Smart et al. (2010), we utilized the values of M_* therein. For the other targets, we derived absolute *K* magnitudes from the distance estimates and we obtained M_* from the mass-luminosity calibration of Delfosse et al. (2000). For all the program stars, the Bayless & Orosz (2006) mass-radius relation was then employed to calculate R_* . For completeness, metallicity [Fe/H] estimates are provided using the Johnson & Apps (2009) calibration in the plane $V - K - M_K$, where ap-

plicable and only for objects with trigonometric parallaxes, along with effective temperature T_{eff} values from the Casagrande et al. (2008) *M* dwarfs ($V - K$)- T_{eff} calibration. All the above characteristics of our sample are summarized in Table 3. For each target, the same Table also reports relevant information on flaring activity (obtained from SIMBAD) and activity indicators, i.e., $H\alpha$ equivalent widths measurements.

4 RESULTS

4.1 Photometric precision

Accurately gauging the short- and medium-term photometric precision for our red dwarfs sample, as a function of the characteristics of the instruments adopted and of the details of the methods of differential photometry utilized in the analysis, and including meaningful estimates of the degree of correlated (red) noise in the data, is of fundamental importance. The short-term precision (as defined below) is the quantity that ultimately has the most relevant impact on the probability of detecting a transit signal, and of determining its statistical significance. The medium-term precision is the quantity that allows one to gather insight on different timescales of variability which are more likely to be intrinsic to the target, such as surface activity. As is usual practice, we operationally define the photometric precision of a given target monitored with one of our instruments as the RMS of a differential light curve (for one ob-

Table 3. Characteristics of the M dwarf sample.

| ID | LHS | GJ | RA (hh:mm:ss) | DEC (dd:mm:ss) | d (pc) | V | J | K | M_V | M_K | M_\star (M_\odot) | R_\star (R_\odot) | T_{eff} (K) | [Fe/H] (dex) | Flare star | H α EW (\AA) |
|----|------|-------|------------------|-------------------|-----------------------------|--------------------|-------|-------|-------|-------|----------------------------|----------------------------|-------------------------|-----------------|---------------|--|
| 1 | 1104 | ... | 00:35:53.1 | +52:41:13.7 | 24.7 \pm 1.3 ^a | 12.54 ^a | 8.93 | 8.09 | 10.58 | 6.13 | 0.44 | 0.45 | 3317 | 0.07 | n | ... |
| 2 | 1475 | 119 | 02:56:34.4 | +55:26:14.0 | 16.7 \pm 1.4 ^a | 10.48 ^a | 7.43 | 6.59 | 9.37 | 5.48 | 0.56 | 0.57 | 3620 | ... | n | -0.534 ^b |
| 3 | 228 | ... | 07:16:27.7 | +23:42:10.4 | 42.4 \pm 2.0 ^a | 15.53 ^a | 12.02 | 11.30 | 12.39 | 8.17 | 0.12 | 0.14 | 3424 | -1.27 | n | ... |
| 4 | 243 | ... | 08:03:06.1 | +34:56:54.8 | 24.4 \pm 0.7 ^a | 16.09 ^a | 11.51 | 10.74 | 14.15 | 8.81 | 0.09 | 0.11 | 2986 | -0.67 | n | ... |
| 5 | 1976 | ... | 08:03:19.5 | +52:50:38.1 | 24.8 \pm 3.1 ^a | 11.38 ^a | 8.06 | 7.24 | 9.407 | 5.26 | 0.58 | 0.58 | 3472 | 0.29 | n | ... |
| 6 | 6158 | 3522 | 08:58:56.3 | +08:28:25.9 | 6.8 \pm 0.1 ^c | 10.92 ^c | 6.51 | 5.69 | 11.76 | 6.53 | 0.36 | 0.37 | 3023 | 0.51 | y | +2.76 ^d |
| 7 | 269 | ... | 09:29:11.0 | +25:58:09.3 | 16.7 \pm 1.3 ^e | 16.43 ^b | 10.91 | 9.96 | 15.32 | 8.85 | 0.11 | 0.14 | 2697 | ... | n | ... |
| 8 | 2220 | 3585 | 10:06:43.8 | +41:42:52.6 | 20.7 \pm 1.2 ^f | 11.31 ^g | 8.21 | 7.40 | 9.73 | 5.82 | 0.49 | 0.50 | 3607 | -0.21 | n | ... |
| 9 | 283 | 3612 | 10:35:26.9 | +69:26:58.8 | 13.2 \pm 0.7 ^h | 11.95 ^h | 7.90 | 7.16 | 11.35 | 6.56 | 0.35 | 0.37 | 3175 | 0.13 | n | -0.219 ^b , +0.13 ^d |
| 10 | 2472 | 452.1 | 11:54:07.9 | +09:48:22.8 | 11.3 \pm 0.5 ^a | 12.81 ^a | 8.70 | 7.87 | 12.54 | 7.60 | 0.20 | 0.22 | 3120 | -0.33 | y | +1.248 ^b |
| 11 | 360 | ... | 13:46:55.5 | +05:42:56.3 | 56.2 \pm 9.5 ^a | 15.22 ^a | 12.39 | 11.66 | 11.47 | 7.87 | 0.28 | 0.29 | 3858 | ... | n | ... |
| 12 | ... | 569B | 14:54:29.2 | +16:06:03.8 | 9.7 \pm 0.2 ^f | 10.38 ^g | 6.63 | 5.77 | 10.45 | 5.84 | 0.48 | 0.49 | 3247 | 0.37 | y | +0.852 ^b |
| 13 | 417 | 623 | 16:24:09.3 | +48:21:10.4 | 8.1 \pm 0.08 ^f | 10.27 ^g | 6.64 | 5.91 | 10.73 | 6.37 | 0.38 | 0.40 | 3359 | -0.14 | n | -0.237 ^b |
| 14 | 3343 | 4040 | 17:57:50.9 | +46:35:19.1 | 14.6 \pm 0.5 ^a | 11.68 ^g | 7.85 | 7.00 | 10.85 | 6.17 | 0.40 | 0.41 | 3219 | 0.25 | n | -0.215 ^b , +0.15 ^d |
| 15 | 3445 | 9652A | 19:14:39.1 | +19:19:03.7 | 17.9 \pm 0.7 ^a | 11.59 ^g | 7.58 | 6.81 | 10.32 | 5.54 | 0.41 | 0.42 | 3179 | 0.69 | y | +5.4 ^d , +5.7 ⁱ |
| 16 | 528 | 1271 | 22:42:38.7 | +17:40:09.2 | 17.4 \pm 0.7 ^a | 11.76 ^g | 8.06 | 7.18 | 10.55 | 5.98 | 0.43 | 0.44 | 3260 | 0.26 | n | ... |
| 17 | 534 | 4311 | 23:06:35.6 | +71:43:25.5 | 17.3 \pm 5.2 ^e | 11.75 ^l | 8.34 | 7.56 | 10.56 | 6.37 | 0.37 | 0.39 | 3445 | ... | n | ... |
| 18 | 1721 | 1074 | 04:58:46.0 | +50:56:37.8 | 19.3 \pm 0.9 ^f | 11.06 ^l | 7.90 | 7.04 | 9.63 | 5.61 | 0.53 | 0.54 | 3540 | -0.01 | n | -0.452 ^b |
| 19 | 370 | ... | 14:20:53.1 | +36:57:16.8 | 21.7 \pm 1.7 ^e | 16.17 ^h | 11.05 | 10.25 | 14.49 | 8.57 | 0.13 | 0.16 | 2829 | ... | n | ... |
| 20 | 306 | 3668 | 11:31:08.3 | -14:57:21.1 | 11.8 \pm 2.6 ^a | 14.19 ^g | 9.36 | 8.50 | 13.83 | 8.14 | 0.12 | 0.14 | 2889 | -0.05 | n | ... |
| 21 | ... | 1167A | 13:09:34.9 | +28:59:06.6 | 10.8 \pm 0.6 ^a | 14.52 ^a | 9.48 | 8.61 | 14.35 | 8.44 | 0.12 | 0.14 | 2832 | -0.08 | y | +4.82 ⁱ |
| 22 | 2686 | ... | 13:10:12.6 | +47:45:18.4 | 10.3 \pm 0.5 ^a | 14.16 ^g | 9.58 | 8.69 | 14.09 | 8.62 | 0.09 | 0.11 | 2951 | -0.47 | n | ... |
| 23 | 2719 | ... | 13:20:27.0 | -03:56:14.5 | 26.9 \pm 2.5 ^a | 15.60 ^g | 11.28 | 10.48 | 13.45 | 8.33 | 0.15 | 0.17 | 3058 | -0.58 | n | ... |

^a Trigonometric parallax / V magnitude after Smart et al. 2010 and references therein^b Gizis, Reid & Hawley 2002^c Trigonometric parallax / V magnitude after Henry et al. 2006^d Walkowicz & Hawley 2009^e Photometric parallax / V magnitude after Lépine & Shara 2005^f Trigonometric parallax from Hipparcos data, after Van Leeuwen 2007^g V magnitude from ASCC-2.5 catalogue, after Kharchenko 2001^h Trigonometric parallax / V magnitude after Reid & Cruz 2002ⁱ Shkolnik et al. 2009^l TASS Mark IV photometric catalogue, version 2, after Droege et al. 2006

serving night or for the whole time interval of the observations) obtained with any of the four methods ($m1$ through $m4$) defined in § 2. To first order, this corresponds to the uncertainty of each data point.

4.1.1 Global analysis

Our first goal is to determine the precision of our photometric measurements on a nightly basis (short-term precision) and over the whole temporal length of the observations (medium-term precision). For each target, we determine the short-term photometric precision of the data by computing the intra-night RMS values of eight light curves: four derived from the nightly light curves and four extracted from the full-period light curves. We determine the medium-term precision in our dataset by computing the global RMS values of the four full-period light curves.

For the purpose of computing the RMS values, we utilized unbinned light curves for the 25-cm and 40-cm telescopes, while we utilized binned light curves (at 1.5 min) for the 81-cm telescope. The binning of the 81-cm telescope data is necessary in order to homogenize them with the typical time sampling of the other two telescopes, and more importantly to suppress the effects of atmospheric scintillation, which usually affects to a significant degree very short (few seconds) exposures.

In the three panels of Figure 1 we show the distributions of the

mean short- and medium-term RMS values for each target, for the various methods. Visual inspection of the plots already shows qualitatively two relevant results: the apparently good agreement between different methods for differential photometry (with or without detrending), both in the short- and medium-term regimes, and the fact that the medium-term photometric precision appears degraded with respect to the short-term precision. We put the discussion on more firm statistical grounds by performing a comparison between the various RMS distributions based on the Kolmogorov-Smirnov (K-S) test, which measures the probability P_{K-S} of any two distributions being statistically indistinguishable.

First, we perform the K-S test between the four distributions within each panel of Figure 1, to gauge statistical differences in the RMS distributions between the $m1$ through $m4$ analysis methods, separately for the short- and medium-term regimes. The results, expressed in terms of P_{K-S} , are summarized in Table 4.

Next, the K-S test is performed to evaluate the differences between the RMS distributions in the short- and medium-term regimes. Given the results shown in Figure 1 (i.e., methods $m1$ through $m4$ provide the same answers), we show here only for simplicity the comparison between the RMS distributions of method $m1$ from one panel with all other distributions in the other panels. The corresponding values of P_{K-S} are summarized in Table 5.

Finally, the K-S test is performed to evaluate the differences between the RMS distributions from data obtained with different

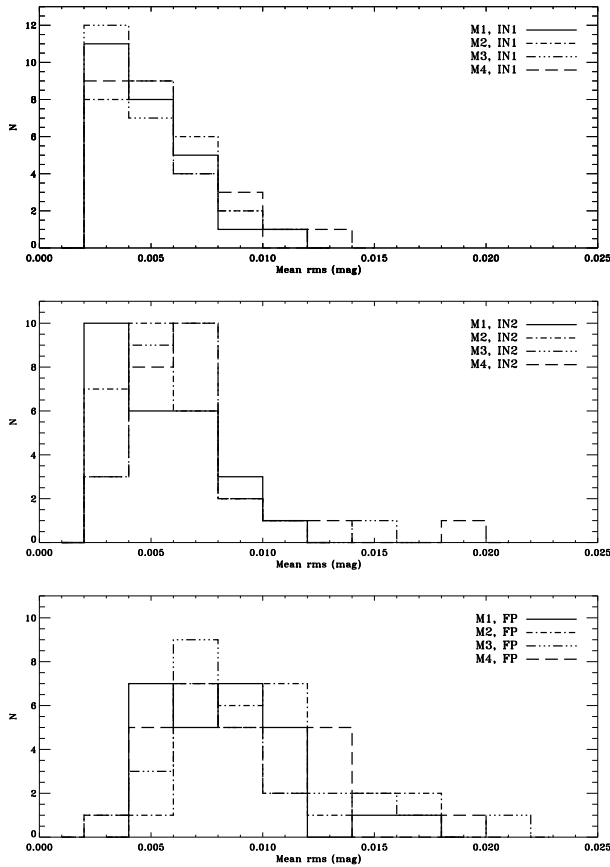


Figure 1. Distribution of the mean RMS for each target. For each of the four differential photometry methods, the panels show: the mean intra-night RMS distribution IN1 for the sample (top), the mean intra-night RMS distribution IN2 extracted from a full-period light curve for each target (center), and the full-period RMS distribution FP for the sample (bottom).

Table 4. K-S test results (1).

| m1-m2 | m1-m3 | m1-m4 | m2-m3 | m2-m4 | m3-m4 |
|------------------------|-------|-------|-------|--------|-------|
| Figure 1, upper panel | | | | | |
| 0.992 | 0.992 | 0.992 | 0.674 | 0.9928 | 0.674 |
| Figure 1, middle panel | | | | | |
| 0.992 | 0.138 | 0.258 | 0.440 | 0.258 | 0.999 |
| Figure 1, lower panel | | | | | |
| 0.138 | 0.674 | 0.674 | 0.440 | 0.258 | 0.992 |

telescopes. The corresponding values of P_{K-S} are summarized in Table 6.

The results from the global short-term and medium-term photometric RMS analysis based on the K-S test highlight the following:

- 1) the use of a range of instrumental setups does not impact significantly the typical performance in the photometry;
- 2) the differential photometry methods (without detrending) adopted within the pipeline provide consistently similar results;
- 3) the similarity between the different light curve RMS values with and without detrending indicate that our data are not particularly affected by linear systematic trends that can be easily identified and removed, such as atmospheric extinction, detector efficiency, or PSF changes over the detector, for which algorithms like SysRem are very effective;

Table 5. K-S test results (2).

| m1-m1 | m1-m2 | m1-m3 | m1-m4 |
|---|--------|-------|--------|
| upper panel (Fig. 1)- middle panel (Fig. 1) | | | |
| 0.258 | 0.138 | 0.012 | 0.031 |
| upper panel (Fig. 1)- lower panel (Fig. 1) | | | |
| 0.001 | 2e-8 | 4e-5 | 0.0002 |
| middle panel (Fig. 1)- lower panel (Fig. 1) | | | |
| 0.031 | 0.0002 | 0.031 | 0.013 |

Table 6. K-S test results (3).

| 25cm-40cm | 25cm-81cm | 40cm-81cm |
|-----------|-----------|-----------|
| 0.315 | 0.565 | 0.397 |

4) the differences between the short- and medium-term photometric precision suggest that correlated noise (astrophysical in nature, or not) becomes important on timescales longer than those of one observing session (one night). For example, the degradation in precision seen in the bottom panel of Fig. 1 could be ascribed in part to flat-fielding errors and/or to pointing errors and telescope drifts, the latter effectively reducing the number of reference objects used to perform differential photometry on all the nights at once (we recall that an object can be used as comparison star only if it is detected in every frame, and the probability that a star is lost in one or more frames increases with the time span covered by the observations).

In summary, the typical short-term photometric precision is ~ 5 mmag and the typical medium-term photometric precision is ~ 9 mmag. The former result for the M dwarf sample is in excellent agreement with the findings of Damasso et al. (2010), who had focused their analysis on a small number of stars more similar to the Sun.

4.1.2 Correlated (red) noise analysis

The RMS of the whole light curve can be assumed to be the uncertainty of each data point under a fundamental hypothesis: the photometric measurements are assumed to be uncorrelated (white noise regime). At the millimag level and in a high-cadence time series this is generally untrue. There are many effects that can produce a correlated photometric measurements (red noise regime): changing airmass, atmospheric conditions, telescope tracking (and relative flat field errors) and the intrinsic variability of the targets. These effects introduce some covariance between data points.

The presence of red noise can have a rather significant impact on the statistical analysis of the data. As an example, let us consider a light curve, with no evident variability, consisting on N flux measurements f_i in a fixed time interval, with uncertainties for each data point σ_i equal to the RMS of the whole light curve σ_0 . We calculate the mean of the N flux measurements f_{mean} . The uncertainty on f_{mean} , $\sigma_{f_{mean}}$, is then the error of the mean of f_i . Using the expression for the standard deviation of the mean under the assumption of white noise (σ_w), this uncertainty is:

$$\sigma_{f_{mean}} \equiv \sigma_w = \frac{\sigma_0}{\sqrt{N}}. \quad (2)$$

We note as the uncertainty on f_{mean} decreases with the square root of the number of points N .

The equivalent of Eq. 2 in presence of red noise is:

$$\sigma_{f_{mean}} \equiv \sigma_t = \sqrt{\sigma_w^2 + \sigma_r^2} = \sqrt{\frac{\sigma_0^2}{N} + \frac{1}{N^2} \sum_{i \neq j} C_{ij}}, \quad (3)$$

where the C_{ij} 's are the covariance coefficients between the i -th and j -th measurements (e.g., Pont et al. 2006).

Now, we can estimate σ_t from the light curves, taking in account the red noise, following the methodology described in Pont et al. (2006), and then determine the red noise component from Eq. 3:

$$\sigma_r = \sqrt{\frac{1}{N^2} \sum_{i \neq j} C_{ij}} = \sqrt{\sigma_t^2 - \frac{\sigma_0^2}{N}}. \quad (4)$$

For each star in our sample, we computed σ_t over an interval $\delta t = 30$ min, and repeated the calculations using the light curves from the four intra-night methods. We decided to investigate the red noise contribution to the error budget over this time interval, as an illustrative example. Note that this interval actually corresponds to a significant fraction of the typical transit duration for few-days period planets orbiting mid and late M dwarfs, and thus it's of particular interest for the purpose of this study. We show in Figure 2 the various contributions to the photometric error budget in our dataset, expressed as a function of the target J mag. The results shown correspond to the error analysis for the light curves obtained using method $m1$. The outcome of this specific study is only marginally dependent on the chosen method for differential photometry, as we discuss below. Panel *a* of Figure 2 shows the expected trend of increasing σ_0 with magnitude in the data. Similarly, panel *b* emphasizes a positive correlation of σ_w with magnitude, obviously related to photon noise. This effect is also expected, as the exposure times (see § 2) were chosen so as to guarantee a high $S/N > 100$ for each object, based on the theoretical noise estimate in Eq. 3 of Damasso et al. (2010). Panel *c* shows a weak inverse trend of σ_r with J mag, with decreasing red noise contribution for fainter objects. Again, this is expected because for faint objects σ_w dominates the total error budget, and σ_r becomes increasingly more difficult to determine at the faint end. Finally, panel *d* shows how the total photometric error σ_t in the binned data behaves as a function of J mag due to the combination of correlated and uncorrelated noise terms.

Figure 3 shows, for the whole sample, the behaviour of σ_t (triangle) and σ_w (square) as a function of the number of flux points in a bin (or equivalently, time length of the interval δt). In this case the range of points corresponds to δt ranging from 5 to 90 minutes. The plot highlights that the total noise is influenced by the correlation of the data points mainly on short time scale (small N), while the red component significantly decreases at longer time scales. The noise σ_t , globally, follow a $1/\sqrt{N}$ relation, as it is expected in a regime where the white noise is dominant.

It is furthermore worth mentioning how the typical uncertainties over the average of the time intervals considered here, taking into account the red noise, are 1.4 mmag, 1.6 mmag, 1.2 mmag, and 1.4 mmag for photometric methods $m1$ through $m4$, respectively. This corresponds to values which are 1.3 times, 1.5 times, 1.2 times, and 1.3 times larger than a pure white noise regime. Based on a K-S test, such differences are deemed significant with confidence levels of 94.0%, 99.1%, 95.4%, and 99.9%, respectively. As opposed to the results obtained in § 4.1.1, where we simply used the global light curve RMS as a comparison metric, this more in-depth analysis underlines how the detrending algorithms are actually useful for the purpose of suppressing some of the correlations present in our data.

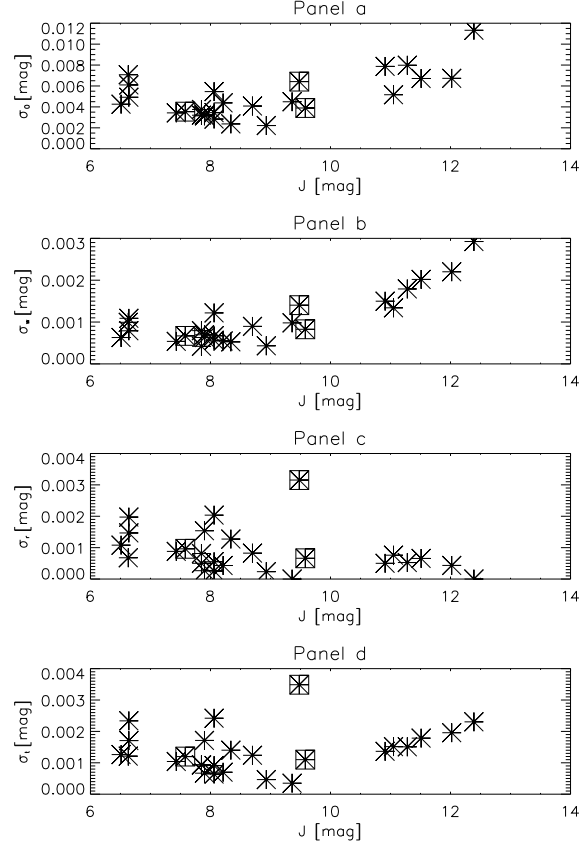


Figure 2. Panel *a*: mean RMS of the unbinned light curves as a function of J mag. Panel *b*: white noise term as a function of J mag. Panel *c*: red noise term as a function of J mag. Panel *d*: the total error term for the binned light curves as a function of J mag. Stars indicated by asterisks framed by a square are objects showing clear signs of activity (see § 4.4 and § 4.3)

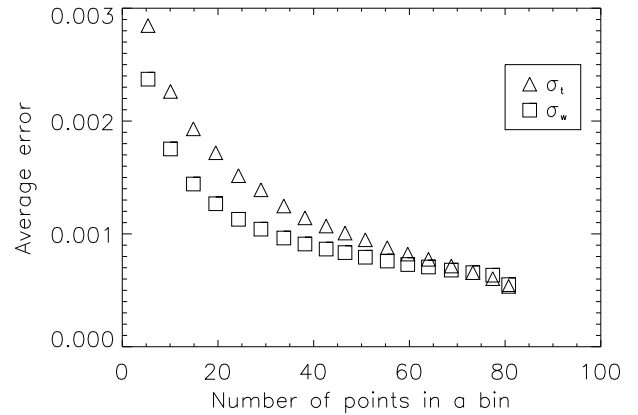


Figure 3. The behaviour of σ_t and σ_w vs number of points in time bins

Finally, we note how the red noise analysis can also be used in principle to investigate the intrinsic variability of a target at the millimag level. The points framed by a square in Figure 2 are the three stars in our sample showing clear signs of activity, for which we have observed either flare events or determined their likely photometric rotation period based on the presence of surface inhom-

genities, or both (see § 4.4 and § 4.3). In one case (GJ 1167A), the high levels of red noise could also be seen as an indication of strong activity (i.e. photometric variability) at the millimag level, and on short timescales. Of course, in order to systematically apply this type of analysis to describe stellar activity robust calibration procedures on a statistically significant sample of stars are necessary, together with the help of spectroscopic measurements. This is a challenge we plan to take up in the future, in order to better characterize the global target sample of our upcoming survey, as this might also allow us to reduce the investment in spectroscopic follow-up observations.

4.1.3 On the choice of the comparison stars

When characterizing the sources of correlated and uncorrelated noise in our photometric data, it is reasonable to expect them to at least in part be due to details in the selection of the reference objects. This is all the more so in the case of differential photometry of late-type targets observed with red filters (e.g., Bailer-Jones & Lamm 2003). To test this possibility, for each red dwarf in our sample we calculated an ‘average’ colour index $V - K$ of the references (using the magnitudes of the NOMAD catalog) and we investigated whether the total intra-night light curve RMS, the white noise, and the red noise contributions showed any significant dependence on colour differences between the red M dwarfs and the typically bluer sets of comparison stars. In parallel, we investigated the possible dependence of correlated and random noise on the average number of comparison stars used for each target, which could also play a role to some degree (especially if one or more of the comparison stars were to show variability).

The left three panels of Fig. 4 show the average red noise (top), white noise (middle), and total RMS (bottom) for the sample as a function of the difference between the colour index of the target and the average color index of the corresponding comparison stars ($V_r - K_r - (V - K)$). The data are binned along the X-axis and error-bars correspond to the dispersion of the values in a bin (the right-most bin contains only two stars). No evident trends with colour index can be found. In the right three panels of Fig. 4 the same quantities are plotted as a function of the average number of comparison stars for each red dwarf in the sample. Even in this case, there is no evident correlation. On the time scale of one observing night, the number of comparison stars or colour-dependent effects such as atmospheric extinction do not appear to impact to any significant extent our measurements. This is in line with, e.g., the analysis of Bailer-Jones & Lamm (2003) and Irwin et al. (2011). The same considerations may not hold in case of our full-period photometry, which is more prone to being affected by other sources of systematic errors, including possible dependency on colour-related effects (e.g., flat-fielding errors), as already mentioned in § 4.1.1. An in-depth analysis to search for colour-dependent effects in the full-period light curves will be the objective of future work.

We also looked at the possibility of evaluating the impact on the noise levels by forcing the choice of red stars as comparisons. We analyzed the fields of GJ 1167A and GJ 9652A, with common proper motion companions at $\sim 3'$ and $\sim 42''$, respectively. Due to their faintness (at V-band they are 2-3 mag fainter than the primaries), GJ 1167B and GJ 9652B are not selected as comparison objects by any of the four intra-night differential photometry methods. By forcing their inclusion in the reference sets for both targets, no appreciable differences in either correlated or random noise levels can be observed, due to the significant number (> 10) of much brighter references selected by the pipeline in all cases.

While this preliminary analysis has not uncovered significant color-dependent effects which could be ascribed to the choice of references, we are aware that prescriptions within TEEPEE should still be included for handling comparison sets with average colour indexes not vastly different from that of the target, particularly when it comes to reducing data over a long period of observations. Recipes have already been identified by other programs targeting specifically large samples of M dwarfs (e.g., Irwin et al. 2011), which are fine-tuned to the specific observing strategy, observational setup, and sample size. Such a careful data treatment will be applied in the future to our survey data.

4.2 Photometric variability: periodicity analysis

After the characterization of the photometric noise properties for the M dwarfs observed during the pilot study, we describe here the key elements of the analysis segment devoted to the astrophysical characterization of the stars themselves. We look for signals in the data which are periodic in nature, and which would indicate either the presence of a transiting companion or which could be interpreted as intrinsic to the target (e.g., due to chromospheric activity). In separate works (Damasso et al. 2011; Giacobbe et al. 2012 in prep.), the search tools applied here to our program stars were used to characterize the nature of tens of newly discovered variable stars in the target fields.

4.2.1 Searching for transit-like events

While showing an exact periodicity, a highly non-sinusoidal transit event cannot be modelled efficiently using standard approaches based on finite sums of sinusoidal components, such as the Discrete Fourier Transform method (e.g., Deeming 1975), or on period-finding techniques which minimize the scatter in smoothed light curves, such as the Phase Dispersion Minimization algorithm (e.g., Stellingwerf 1978). As is now common practice, in order to detect periodic transit events in our data we use a method of least squares fits of step functions to a folded signal corresponding to a grid of trial periods, as realized in the Box-fitting Least Squares (BLS) algorithm (Kovács et al. 2002).

In the analysis (performed in IDL with the exception of a C++ implementation of the BLS period search), we utilized (for each photometric reduction method) the intra-night light curves of each target without σ -clipping, as (partial) transit events might in principle be recognized as clusters of outlier points and removed from the datasets. All light curves were inspected for transit-like signals using a dense grid of 10000 trial periods in the range 0.4-5.0 days. We divided the folded time series into 300 bins and we evaluated the signal residue (i.e., the BLS power spectrum) of the time series using these binned values. We fixed the fractional transit length in the range of 0.1-0.01. The study of the BLS spectra does not show any significant periodicity within the period range investigated, for all objects in our sample. This is not unexpected, given the very small number of targets included in the pilot study, due to standard considerations of geometric transit probability.

4.2.2 Characterizing stellar rotation

For most of our program stars, the photometric data collected during our one-year long observing campaign, covering a typical timespan of ~ 2 months, can be used to directly measure the stellar rotation periods if quasi sinusoidal variations in the broad-band

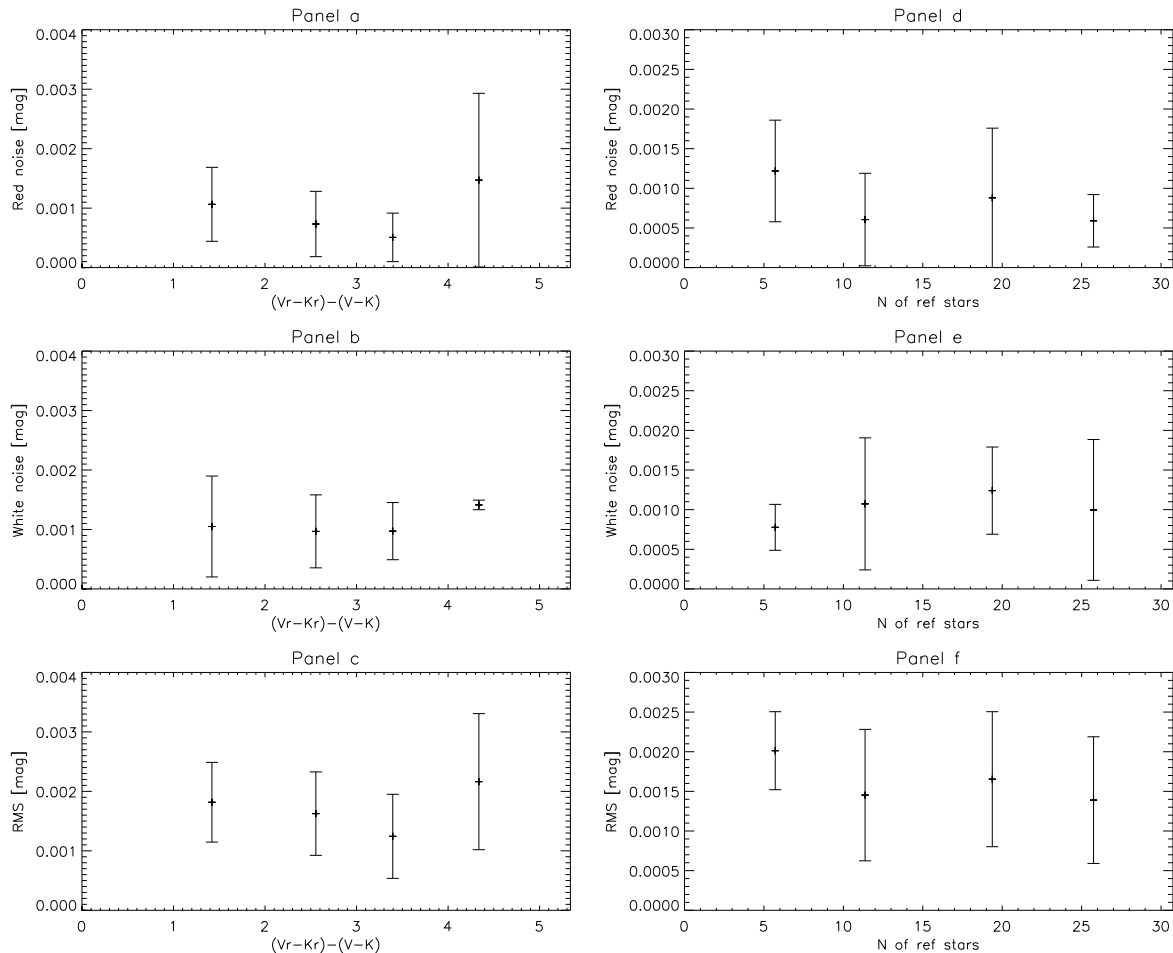


Figure 4. Left: Red noise (top), white noise (middle), and total RMS (bottom) for the sample as a function of the difference $(Vr-Kr)-(V-K)$ between the colour index of the target and the average color index of the corresponding comparison stars. Right: The same quantity is plotted as a function of the average number of comparison stars for each red dwarf in the sample.

photometric signal are detected, under the assumption that it is produced by short- and medium-lived spots on the stellar photosphere.

In order to reveal the presence of presumably starspots-induced rotational modulation in the full-period differential photometric datasets (extracted with the $m2$ and $m4$ methods) of our targets, we looked for agreement between two different periodicity search algorithms (and limiting our analysis to the determination of the most significant frequency). Both algorithms produced essentially the same results when applied on each of the two light curves, making our conclusions more robust. In the following discussion we present the results of the period-search analysis as applied to the light-curve obtained with the $m4$ method.

The first tool utilized is the PERIOD04⁶ software (Lenz & Breger 2005), which performs Discrete Fourier Transforms (DFT) of a time series and is used routinely in asteroseismology work (e.g., Aerts et al. 2010). The second method solves directly a linear Least Squares problem: the data are folded according to a grid of different trial periods and fit to a sine function, and at each step the reduced chi-square χ^2 is evaluated. While in the Fourier analysis the significant periods correspond to peaks in the amplitude spectrum, in a periodogram obtained with the second method the best-fit

period will correspond to the trial value which minimizes χ^2 . This approach has been adopted by Irwin et al. (2011) to search for rotation periods in the M dwarf sample of the MEarth survey.

We found that our program stars can be divided in three main groups: *a*) targets which do not show any significant periodicity, *b*) targets for which the power spectra show the existence of several possible periodic signals, but with low significance, and *c*) stars showing one significant frequency in the periodogram which can be reliably interpreted as the star spinning frequency (2 objects in particular, $\sim 10\%$ of the targets).

Here we present the results concerning the determination of the rotation periods of these two targets, LHS 3445 (a.k.a. GJ 9652A) and GJ 1167A. In order to gather independent circumstantial evidence for their periodicity being due to rotation, as observed in our photometric data. We downloaded archival high-resolution spectra of both targets obtained by Shkolnik et al. (2009) with the High Resolution Echelle Spectrograph (HIRES) on the Keck 1 telescope, and we analyzed them to provide an estimate of the projected rotational velocity $v \sin i$. In short, the $v \sin i$ values for the stars are measured from the stellar line widths via a cross-correlation technique which employs as a template a high-resolution spectrum of a slow rotating star of similar spectral type and known projected rotational velocity (see, e.g., Reid & Mahoney 2000). The width

⁶ <http://www.univie.ac.at/tops/Period04/>

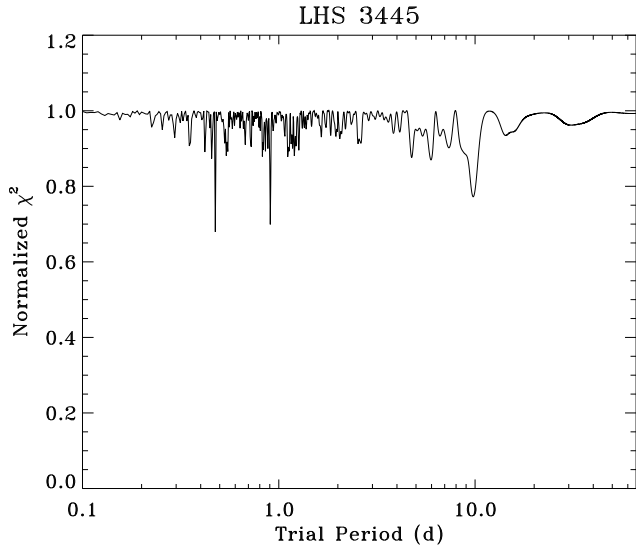


Figure 5. The search for periodicities in the full set of the photometric data for the dM star LHS 3445 revealed the existence of a signal with period $P=0.4752812$ days (corresponding to the absolute minimum in this periodogram).

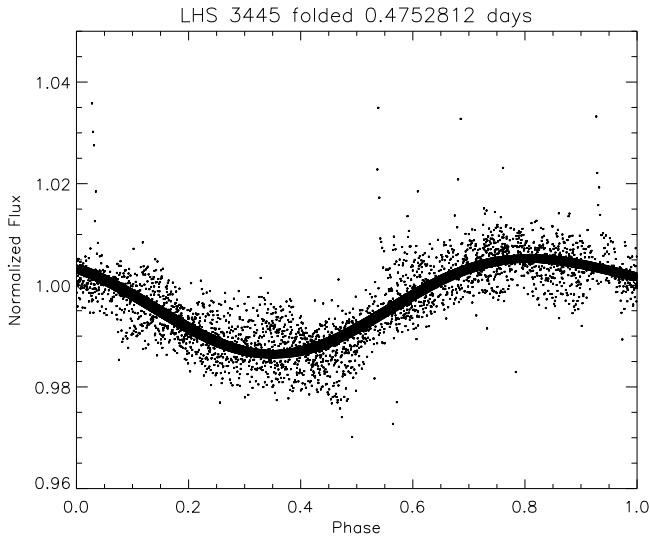


Figure 6. Photometric data for the dM star LHS 3445 folded according to its probable rotation period $P=0.4752812$ days. Overplotted is the best-fit single-spot model described in § 4.3

of the peak in the cross-correlation function is dependent on the line profiles of both template and target object. We used a HIRES spectrum of the star GJ 402 (spectral type dM5) as the slowly rotating template. This spectrum is used to create artificially broadened profiles, with an IDL code that implements the prescription of Gray (2008), and the width of the cross-correlation function (CCF) peak between the unbroadened template and its broadened version is calibrated for a set of rotation speeds. The maximum in a CCF peak vs. $v \sin i$ plot will correspond to the best-fit projected rotational velocity for the target. For our analysis we chose the echelle order covering the spectral range 7370-7490 Å, which is free of TiO bands and telluric lines which would make the analysis difficult.

The star LHS 3445 is included in the samples analyzed by Shkolnik et al. (2009) and Walkowicz & Hawley (2009), and it is

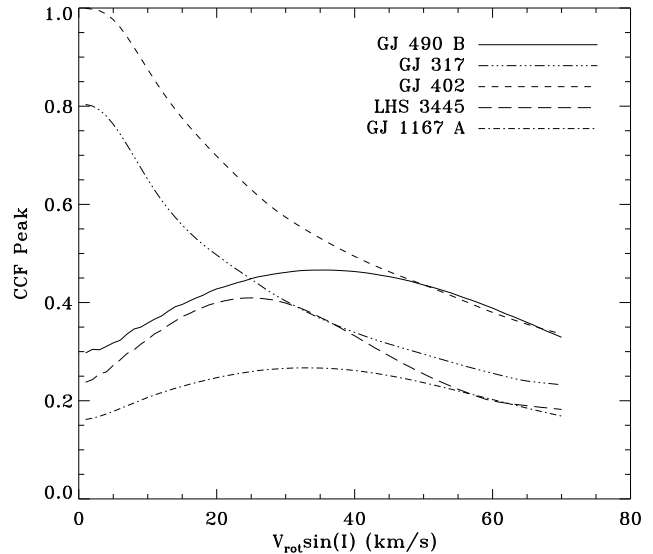


Figure 7. Cross-correlation function (CCF) peaks as a function of the projected rotational velocity $v \sin(i)$ for two of our dM targets, LHS 3445 and GJ 1167A, and other *M* dwarfs used as a template (GJ 402) and check stars used to validate the procedure. The maximum values of the CCF peak functions correspond to the projected rotation velocities measured from the spectra taken with the Keck/HIRES echelle spectrograph. LHS 3445 and GJ 1167A appear to be rapid rotators.

known to be an X-ray active star (it has been identified in ROSAT data) and a flare star (see table 3). We observed this target flaring three times, as described in § 4.4. LHS 3445 is also considered a young star: Smart et al. (2010) indicate an estimated age in the range 30-50 Myr, while Shkolnik et al. (2009) suggest an age between 60 and 300 Myr. Fig. 5 displays the calculated periodogram for LHS 3445, showing a minimum occurring at ~ 0.47 days, and this is confirmed by the DFT analysis. This is then to be considered the most probable rotation period. A second minimum is observed very close to the period of 1 day and we discard it as an alias on the basis of the window function. Fig. 6 shows our photometric data folded according to the period $P=0.4752812$ days, revealing a clear sinusoidal-like shape probably due to star spot modulation. A single-spot model (see § 4.3) is overplotted to highlight the consistency of this hypothesis. As shown in Fig. 7, the analysis of the Keck spectrum leads to the best estimation for the projected rotational velocity $v \sin i \sim 25$ km/s. Note in Fig. 7 that the slow rotating star GJ 317 ($v \sin i < 2.5$ km/s; Browning et al. 2010) is used as a check for the goodness of the results for our targets (i.e. we were able to recover its low projected velocity analyzing the HIRES spectrum) together with the star GJ 490 B, known to be a fast rotator ($v \sin i = 41$ km/s; Phan-Bao et al. 2009), for which we recover a high value of $v \sin i$ in agreement with the one found in the literature. Using the stellar radius indicated in Table 3 and the rotation period estimated photometrically, the mean rotational velocity of LHS 3445 results to be 44.7 km/s, which compared to the projected velocity leads us to conclude that the rotation axis is inclined by ~ 34 deg with respect to the line of sight.⁷

The second target that shows a clear low-amplitude sinusoidal modulations in the light curve is GJ 1167A. GJ 1167A is an active

⁷ Note that LHS 3445 has an *M* dwarf common proper motion companion, the star LHS 3446. We analysed its light curve, which appears to be not at all variable over the timescale of our observations.

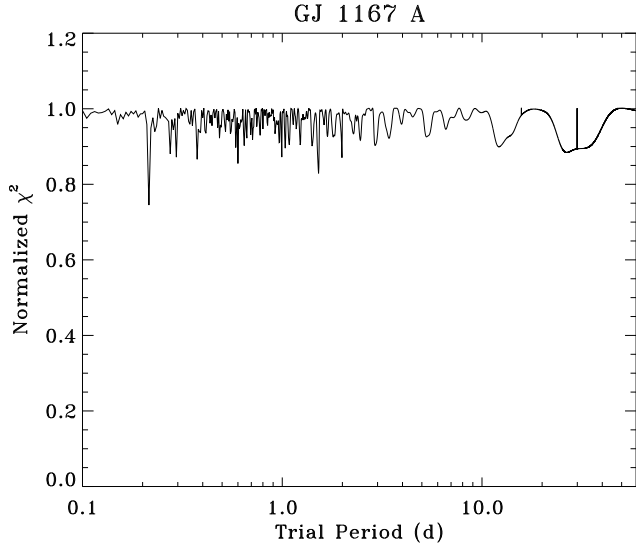


Figure 8. The search for periodicities in the full set of the photometric data for the dM star GJ 1167A revealed the existence of a signal with period $P=0.2151997$ days (corresponding to the absolute minimum in this periodogram).

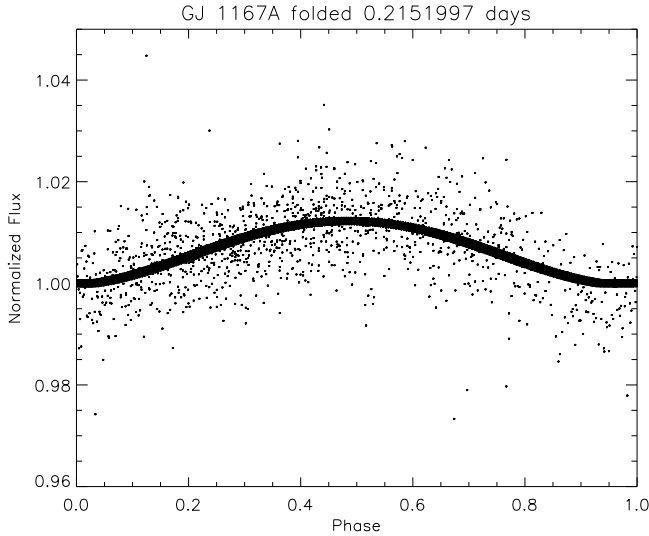


Figure 9. Photometric data for the dM star GJ 1167A folded according to its probable rotation period $P=0.2151997$ days. Overplotted is the best-fit single-spot model described in § 4.3

flare star (but no flares were observed over the timespan of our observations), included in the samples analysed by Shkolnik et al. (2009), who classify it as a young dM4.8 star with an age in the range $60\div 300$ Myr. In Smart et al. (2010) GJ 1167A is reported being a dM4.0 star with a rather uncertain (0.12–10 Gyr) age. Both the DFT and PDM analysis of our photometric data reveals a clear sinusoidal periodic signal corresponding to $P\sim 0.22$ days (the PDM results are shown in Fig. 8). Fig. 9 shows the light curve folded according to this period, with superposed a single-spot model as for LHS 3445 (see § 4.3). The fact that GJ 1167A is a very fast rotator is confirmed by the line broadening analysis of the HIRES spectrum, as shown in Fig. 7. We estimate $v \sin i \sim 33$ km/s. Assuming for this star a radius $R = 0.14R_{\odot}$, our measured photometric rotation period implies a true rotational velocity of 32.9 km/s, which means

we are looking at GJ 1167A virtually perpendicularly to its rotation axis.

Given the high rotational velocities inferred for both LHS 3445 and GJ 1167A, this possibly implies relatively young ages for these stars. Alternatively, the rapid spin period could also be due to tidal synchronization effects if these stars were to be very short-period binaries. Indeed, Smart et al. (2010) hint at the possible binarity of LHS 3445 based on kinematics considerations. We checked the cross-correlation functions obtained from the archival high-resolution Keck/HIRES spectra, looking for evidence of double peaks, which would indicate the presence of the secondary spectrum. No such evidence is found in both cases, thus we tentatively conclude that LHS 3445 and GJ 1167A do not harbor very short-period companions of comparable mass. Naturally, a more aggressive analysis could be carried out, based for example on detailed modeling using improved cross-correlation techniques such as TODCOR (Zucker & Mazeh 1994), aimed at faint companions detection. We plan to pursue this issue further in future work.

4.3 Photometric variability: starspots analysis

On the basis of the results described in the previous paragraph, we attempted at modeling the observed photometric variability of LHS 3445 and GJ 1167A assuming it is due to a rotating spot on the stellar photosphere. This work must be intended as the first step towards a more detailed model for star spot distribution to be developed in the course of the upcoming long-term photometric monitoring program, which will become a particularly valuable tool to evaluate the impact on the low-mass planet detection thresholds (e.g. Barnes et al. 2011).

The model we developed is based on the work of Makarov et al. (2009). This three-dimensional model describes the flux modulation due to a small circular spot rotating on the stellar surface. We modelled a single circular spot of radius r with its center located at latitude b and longitude l in the frame of reference of the star. The star is assumed rotating around its axis with a differential angular velocity $\vec{\omega}(b)$ which depends on the latitude on the stellar disk, and the spot is assumed rotating at a fixed latitude. The rotation axis is considered tilted by an angle i measured starting from the line of sight ($i = 0$ if the axis is pointing toward the observer; $i = \pi/2$ when the axis is perpendicular to the line of sight). In the model, the flux modulation can be expressed as $\frac{\Delta F}{F} = -f_s \frac{r^2 I(\theta) \cos \theta}{I_{tot}}$, where f_s is the spot contrast with respect to the local surface brightness, r is the spot size in units of the stellar radius ($r \ll 1$), I_{tot} is the integrated intensity flux from the stellar disk, $\theta = \theta(\mathbf{b}, \mathbf{l}(t))$ is the angle between the line of sight and the perpendicular to the star surface passing through the center of the spot (depending upon the epoch of observation), and $I(\theta)$ is the intensity flux emitted at the spot location. Using the Stefan-Boltzmann law $I = \sigma T^4$, the contrast can be approximated by the relation $f_s = 1 - \frac{T_s^4}{T_{ph}^4}$, where T_s and T_{ph} are the mean temperatures of the spot and photosphere respectively. Using literature prescriptions (Barnes et al. 2011), we set the contrast to vary in the range 0.2–0.8.

The parameters kept fixed in the simulation are the I -band limb-darkening coefficients (a quadratic limb-darkening law from Claret (2000) appropriate for M dwarf stars is used to describe the intensity flux distribution on the stellar photosphere) and the orbital period. The free parameters are the inclination angle of the rotation axis, the spot latitude and the initial longitude, and the scalar $f_s \cdot r^2$ that, combining the spot contrast with its surface area, quantifies

Table 7. Results of the star spot model applied to the fast rotators LHS 3445 and GJ 1167A

| Star | i_* (deg) | b (deg) | $f_s \cdot r^2$ |
|----------|----------------|--------------|-----------------|
| LHS 3445 | 26.7 | 20.3 | 0.00027 |
| GJ 1167A | 89.9 | 42.1 | 0.000007 |

the dimming in the light intensity due to the transit of the star spot in front of the observer.

When applied to the dM stars LHS 3445 and GJ 1167A, the model reproduces well in both cases the inclination of the rotation axis, as found from spectro-photometric data: $i_* = 26.7$ deg for LHS 3445, and $i_* = 89.9$ deg for GJ 1167A. The post-fit residuals, having RMS of 4.2 mmag and 6.4 mmag for LHS 3445 and GJ 1167A, respectively, are comparable to the typical RMS precision achieved for the sample (see § 4.1.1), and do not show any additional significant evidence for periodic signals. All best-fit spot model parameters for the two stars are summarized in Table 7, and the corresponding flux modulations are overplotted to the phased photometric data for the two stars in Fig. 6 and Fig. 9.

We note that our choice to fit for the scalar $f_s \cdot r^2$ rather than the individual values for the brightness contrast f_s and the spot radius r is due to the fact that in the Makarov et al. (2009) model these two parameters appear strongly correlated, and attempting to fit for them separately results in very loose constraints on their actual values, and poor overall convergence of the spot model. This effect can be easily understood, as in the disk-integrated stellar flux data the effect of a cold, small spot is difficult to distinguish from the signal produced by one which is warmer and larger. The price to pay in this case, in that we don't directly estimate the spot size and temperature, is minimal, as this exercise, for the purpose of this study, must be intended solely as a consistency check of the interpretation of the rotational modulation for the two stars based on the photometric and spectroscopic data presented above. Possible future developments include the implementation of more sophisticated (single and multiple) spot models, and the detailed assessment of their uncertainties through, e.g., Bayesian statistics.

4.4 Photometric variability: flares analysis

Flaring events, a powerful indicator of the presence of strong stellar magnetic fields, are known to be relatively common among late-type stars, typically lasting between a few minutes up to several hours, and producing increases in the observed flux of up to several magnitudes. While ground-based as well as space-borne long time-series photometric studies of open clusters and in the field over a range of wavelengths (Moffett 1974; Lacy et al. 1976; Audard et al. 2000; Güdel et al. 2003) have begun unveiling some important correlations between flare occurrence rates and stellar characteristics such as mass, age, and activity levels (e.g., Ambartsumyan et al. 1970; Mirzoyan et al. 1989; Kowalski et al. 2009), the physics of flares is still far from being fully understood. Several open questions still need to be properly addressed, which include the details of the energy release, the mechanisms for producing the atmospheric emission, and the understanding of flares on a global scale – how do flare properties (occurrence rates, emission strength, timescales, frequency) correlate with stellar characteristics (mass, age, activity levels)?

Upcoming ground-based photometric surveys such as Pan-STARRS (Kaiser 2004), PTF (Law et al. 2009), and LSST (Abell et al. 2009) will certainly provide the opportunity to

gather flare data for large numbers ($> 10^6$) of stars, sampling wide ranges of flare amplitudes and timescales. However, a potentially important niche for 'classical' flare studies (i.e., those based on the continuous monitoring of single objects) will come as a by-product of those photometric programs, such as MEarth (Nutzman & Charbonneau 2008) or the upcoming survey at OAVdA, targeting large numbers of relatively bright late K and M dwarfs in search of transiting planets. For example, the detailed characterization of the flaring behavior for K and M dwarfs objectives of targeted searches for transiting planets is an important ingredient towards the thorough understanding of the impact a star and its environment might have through time on the habitability of any planet it may harbor which could sustain the presence of liquid water on its surface (e.g., Kastinger et al. 1993; Lammer et al. 2007; Guinan et al. 2009).

Two of the stars included in our pilot study, LHS 3445 and LHS 2686, showed flaring events in the photometry gathered over a period of 66 days and 60 days, respectively. LHS 3445 is classified as UV Cet type flare star (Gershberg et al. 1999), while no information on flaring is available in the literature for LHS 2686. Given the sampling rate of the two light-curves (54 sec and 75 sec, respectively), we were sensitive to flares with decay times larger than ~ 1 min. Visual inspection of the light-curves allowed us to infer decay times of a few minutes ('impulsive' flares. See, e.g., Krautter 1996). As an illustrative exercise of the type of studies that will be possible once observations will be gathered in survey mode, we characterized the events following the approach of Hartman et al. 2011, i.e. by solving a non-linear Least Squares problem with a set of consecutive photometric measurements starting from the time of recorded maximum brightness t_0 and an exponential model function of the type:

$$m_d(t) = A \times \exp(-(t - t_0)/\tau) + m_{d,0}, \quad (5)$$

with adjustable parameters A , the peak magnitude of the flare relative to the non-flaring magnitude, τ , the decay timescale, and $m_{d,0}$, the differential normalized magnitude (see § 2 for its definition) of the star before the flare. The Least Squares solution was obtained with an IDL implementation of the Levenberg-Marquardt method (Levenberg 1944; Marquardt 1963), MPFIT by Craig Markwardt⁸ (Markwardt 2009), and starting guesses for the model parameters A equal to the peak magnitude, $\tau = 0.001$ d, and $m_{d,0}$ equal to the average differential magnitude of each time series. The results are shown in Figure 10. For LHS 3445, two of the three recorded flares occurred within a timespan of 1.2 hrs during the same night, possibly a case of homologous flares (e.g., Martres et al. 1984; Doyle et al. 1990; Ranns et al. 2000).

4.5 Limits to transiting companions

While no transit event has been recorded in our dataset, as reported in § 4.2.1, the photometric measurements obtained for our sample can be utilized to carry out simulations aimed at determining what sensitivity to transiting companions (of given radius and period) we achieved on a star-by-star basis, expressed in terms of easy-to-interpret comparison metrics, such as detection probabilities and phase coverage. These simulation tools, whose application to the data collected during the pilot study we illustrate here, will be of

⁸ Available at <http://purl.com/net/mpfit>. MPFIT is a port of MINIPACK-1 from FORTRAN, and is also available in C and Python

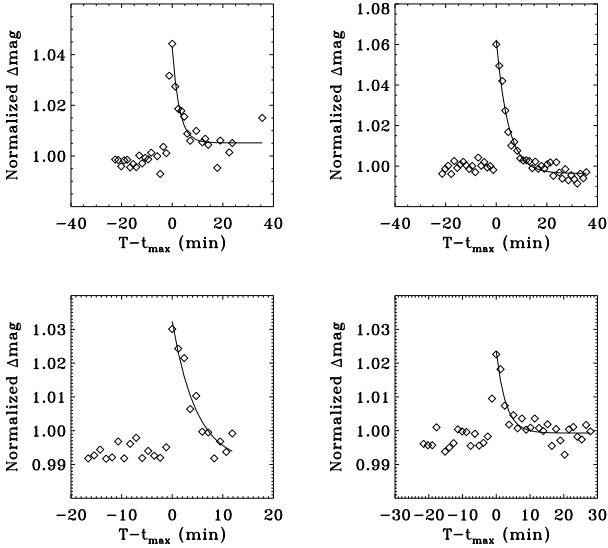


Figure 10. Four flares seen in the LHS 3445 (upper and lower left panels) and LHS 2686 (lower right panel) light curves. In each case, the solid line shows the fit of Equation 5 to the light curve. For LHS 3445, two almost consecutive flares were recorded, with approximately equal decay times of ~ 4.5 min.

great use in the careful prioritization and for the optimization of the scheduling of the targets during survey operations.

In order to evaluate the sensitivity of each of the M dwarfs in our sample to transiting companions of given period and given radius, provided the primary size from Table 3 (or equivalently inducing a transit signal of given depth), a large-scale simulation was performed by injecting synthetic transit signals into the differential light curves (both intra-night and full-period) of our targets (without σ -clipping as in § 4.2.1). We utilized these data under the hypothesis that the procedure adopted to extract it from the raw images does not affect the signal. This simplification assumption is often adopted when dealing with such issues (e.g., Irwin et al. 2011). Furthermore, transit signal injection was performed on all light curves obtained with the four methods for differential photometry described in § 2. We are aware that the specific choices for these elements of the simulation setup can in principle impact our findings to some extent. For example, we are not in a position to estimate quantitatively the effects on our capability to recover transit signals due to the application of trend-filtering algorithms during the production of the differential photometric data in pipeline mode. However, the goal of the present analysis is simply to gauge our ability to detect transit events as a function of the system parameters, given an observed distribution of RMS values for our stellar sample. The present simulation setup is thus appropriate for this purpose, and any in-depth evaluation of, e.g., the quality of the calibration procedures against transit signal detection thresholds goes beyond the scope of this paper. We plan to relax the above assumptions and caveats in a future work in which we will carry out new studies based on a fully consistent end-to-end analysis (including extraction and differential photometry) of modified images in which synthetic transit signals will have been injected already at the pixel level.

The input parameters (and their ranges) to the simulation, which was entirely carried out in IDL, we determined based on considerations taking into account the temporal sampling, total timespan, and typical photometric precision of our data. We generated:

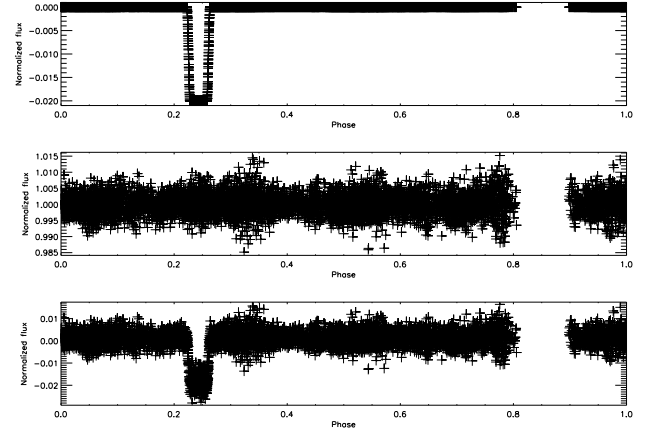


Figure 11. Top: synthetic folded light curve with $t_d = 2\%$ and a period of 1.8468372 days. The times of observation are those of LHS 1976. Center: the actual phased light curve of LHS 1976. Bottom: the combined light curve for LHS 1976

- 1000 random, uniformly distributed periods in the range 0.5 – 5 days;
- 100 random, uniformly distributed phases for each period;
- 4 amplitudes of the transit signal depth t_d (in flux units: 0.02, 0.015, 0.01, 0.005) for each period and phase. The four values of transit depth simulated correspond to companion radii in the ranges 1.5-9.1, 1.3-7.9, 1.1-6.4, and 0.8-4.5 R_{\oplus} , respectively, given the sizes of the primaries from Table 3;
- a fixed orbital inclination $i = 90^\circ$, and perfectly circular orbits ($e = 0.0$);

Consequently, the orbital radius parameter was derived from M_* (see § 3) and from Kepler’s third law under the assumption $M_p \ll M_*$ (Seager & Mallen-Ornelas 2003). We recognize that allowing the inclination to float might change to some extent the details of the detection probability results. A detailed study of the sensitivity to non-central (eventually in the limit of quasi-grazing) transits is left for the future.

With the above simulation setup, 400 000 synthetic transit light curves were generated for each target using the Mandel & Agol (2002) algorithm. For the purpose of this analysis limb-darkening effects are essentially irrelevant and in order to speed up execution they were turned off. For each target, the synthetic transit signals were then injected on both nightly and full-period light curves. The choice of running the simulation for the whole suite of differential photometry methods was driven by the findings of § 4.1.1 and § 4.1.2, thus allowing us to gauge the sensitivity of the transit detection probability to variable photometric precision. This was done in practice by comparing the results obtained by running the BLS algorithm on the synthetic, ‘noise free’ datasets as well as on the combined light curves, with the prescription of discarding datasets in which a transit would have occurred only once.

Figure 11 summarizes the process of injection of a transit signal in a differential light curve. The top panel shows the synthetic folded light curve, without limb-darkening, produced by the Mandel & Agol (2002) formalism for a transit with a fractional depth of 2% and a period of 1.8468372 days. The center panel shows the actual phased light curve of LHS 1976, while the bottom panel shows the combined light curve in phase. The datasets shown in the upper and lower panels are both fed to BLS.

In the analysis with the transit search algorithm of a given light

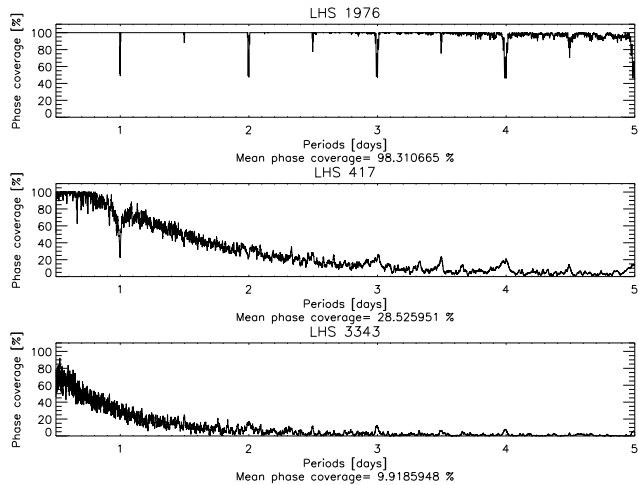


Figure 12. Phase coverage as a function of period of the injected transit signal ($t_d = 2\%$). Top: LHS 1976. Center: LHS 417. Bottom: LHS 3343

curve, BLS was run using 500 period steps in the range $0.5 - 5$ days, the folded time series was divided into 100 bins, and the signal residue (SR) of the time series (see Kovács et al. 2002) was determined using these binned values. We fixed the fractional transit length to lie in the range $0.1 - 0.01$.

As mentioned above, the main results of the simulation are expressed in terms of two simple comparison metrics, which we identified to be the phase coverage and the transit detection probability.

Here we calculate the phase coverage, in a period range of 0.5 to 5 days, for 10000 trial periods. We divide the phased light curve in bins corresponding to 20 min in length (obviously the number of bins changes with the trial period). A single bin is flagged as ‘filled’ (i.e. containing a satisfying number of data points) if at least five points coming from three different nights fall within. The phase coverage (expressed as percentile) represents the relative number of bins that satisfy this condition with respect to the total number of bins.

We define the detection probability as the relative number of periods that are detected by BLS with respect to the total number of injected periods. We considered as detections all those signals for which BLS returned a period T' such that $|T' - T_{in}|/T_{in} < 0.01$, where T_{in} was either the actual period of the injected signal, or half that period, or twice that period. We are aware of the fact that this requirement might be somewhat stringent: In practice we do not consider as detections transits identified with the correct depth, but with an incorrect period due to, e.g., the sampling properties of the light curve. We adopted this more conservative approach to the definition of detection probabilities as a way to partly compensate for the caveats and assumptions of the simulation scenario listed at the beginning of this section.

Figure 12 shows the phase coverage as a function of injected period for a signal with $t_d = 0.02$ for three representative objects in our sample, LHS 1976, LHS 417, and LHS 3343, with very different (from poor to excellent) levels of phase coverage.

For the same three stars, and in the case of differential light curves obtained with method *m3*, Figure 13, Figure 14, and Figure 15 give an overview of all the fundamental ingredients provided in output from the simulation. In every Figure, the top-most four sub-panels (*a*) show, for each of the values of t_d simulated, the original distribution of injected transit signals (solid line) and

that of those signals whose corresponding light curves (synthetic as well as combined) are subsequently fed to BLS (dashed line), both expressed as a function of period. The second set of sub-panels (*b*) shows the fraction of BLS-detected signals in the synthetic datasets (solid line) and in the combined light curves (dashed line). The third set of sub-panels (*c*) shows the distribution of the signal detection efficiency (SDE) parameter both in the case of synthetic light curves (solid line) and for the combined light curves (dashed line). We remind the reader that a value for SDE , which quantifies the statistical robustness of a detected transit-like periodic signal in the language of BLS, is computed as:

$$SDE = \frac{SR_{peak} - \langle SR \rangle}{sd(SR)}, \quad (6)$$

where SR_{peak} is the value of the peak in the signal residue distribution, while $\langle SR \rangle$ and $sd(SR)$ are the mean and the standard deviation of SR over the frequency band tested (see Kovács et al. 2002 for details). Finally, the last set of sub-panels (*d*) shows the distribution of the transit depths of the detected signals as evaluated by BLS from the synthetic light curves (solid line) and from the combined light curves (dashed line).

For all three Figures, sub-panels *a* and *b* clearly illustrate the dependence of transit detection probability on period. As expected, this behaviour is very similar to the trend of phase coverage with period (see Figure 12). Panels *b* also quantify the amount of degradation in detection probability, with respect to the ‘noise-free’ case, when the transit depth approaches the typical photometric precision, even when the phase coverage is very good.

The three sets of sub-panels *c* illustrate how the statistical significance of a detection, as measured by the SDE values, changes with phase coverage and signal depth. The values of SDE can also be used to quantify the probability of a detection being a false positive. The actual behaviour of SDE depends on many factors, some intrinsic to the algorithm (e.g. number of bins, number of trial periods) and others depending on the quality of the data and of the signal (e.g. S/N), however the statistical studies Kovács et al. (2002) indicate a value of $SDE \sim 5$ above which the false positive probability is low ($< 10\%$). Above such value the SDE does not depend on the input parameters of BLS (Figure 5 of Kovács et al. 2002). The plots in Figure 13 show how the typical value of SDE decreases with the amplitude of the signal and with the phase coverage. In Figures 14 and 15 this trend is less evident. This is due to the SDE values fluctuating within a regime where the false positive probability is very high. The fact that many signals are detected with a low SDE highlights the robustness of the BLS algorithm, which is capable of uncovering weak and noisy signals albeit with low statistical confidence.

The analysis of the transit depth distribution, as shown in panel *d*, is a further test of the BLS reliability. Generally BLS provides a good estimate of the signal amplitude, but looking at the three figures an underestimation of the signal amplitude can be noticed. This is due to the initial parameters (number of bins, number of trial periods) of BLS that, in this case (in order to reduce the CPU time calculation), are insufficient to define precisely the ‘border’ of the signal. This effect appears to increase with the phase coverage. This should be explained taking in account that the number of ‘spurious’ points increases with such phase coverage. To verify that this underestimate depends on the input parameters of BLS, we ran the algorithm on our archive data for the transiting planet WASP-3b (Damasso et al. 2010) increasing the number of trial periods to 10000 (in the same range of the simulation) and the number

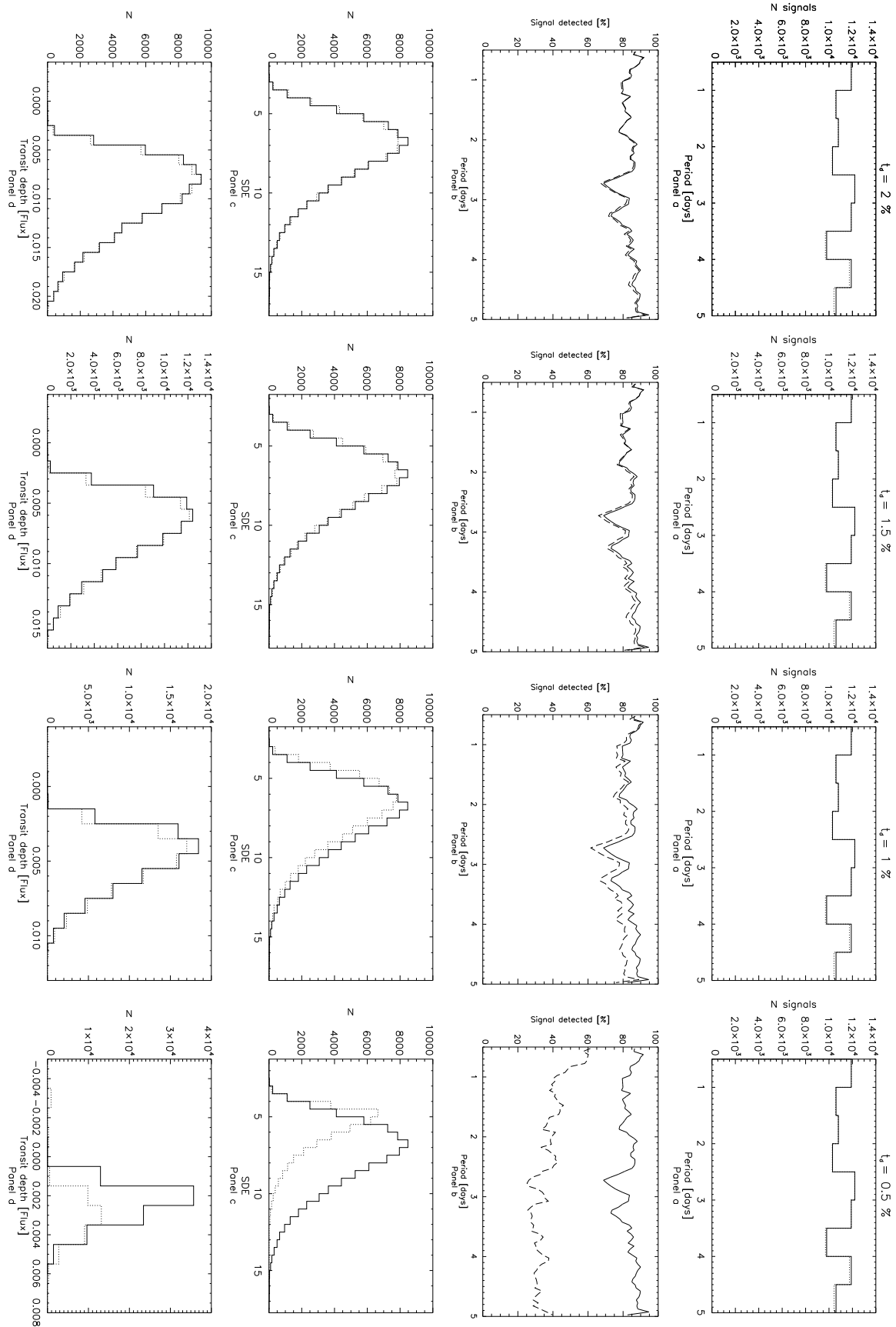


Figure 13. Summary of simulation output for LHS 1976 (see text for details). Panels *a*: number of signals vs period; Panels *b*: detection probability vs period; Panels *c*: SDE distributions; Panels *d*: distributions of transit depths of the detected signals.

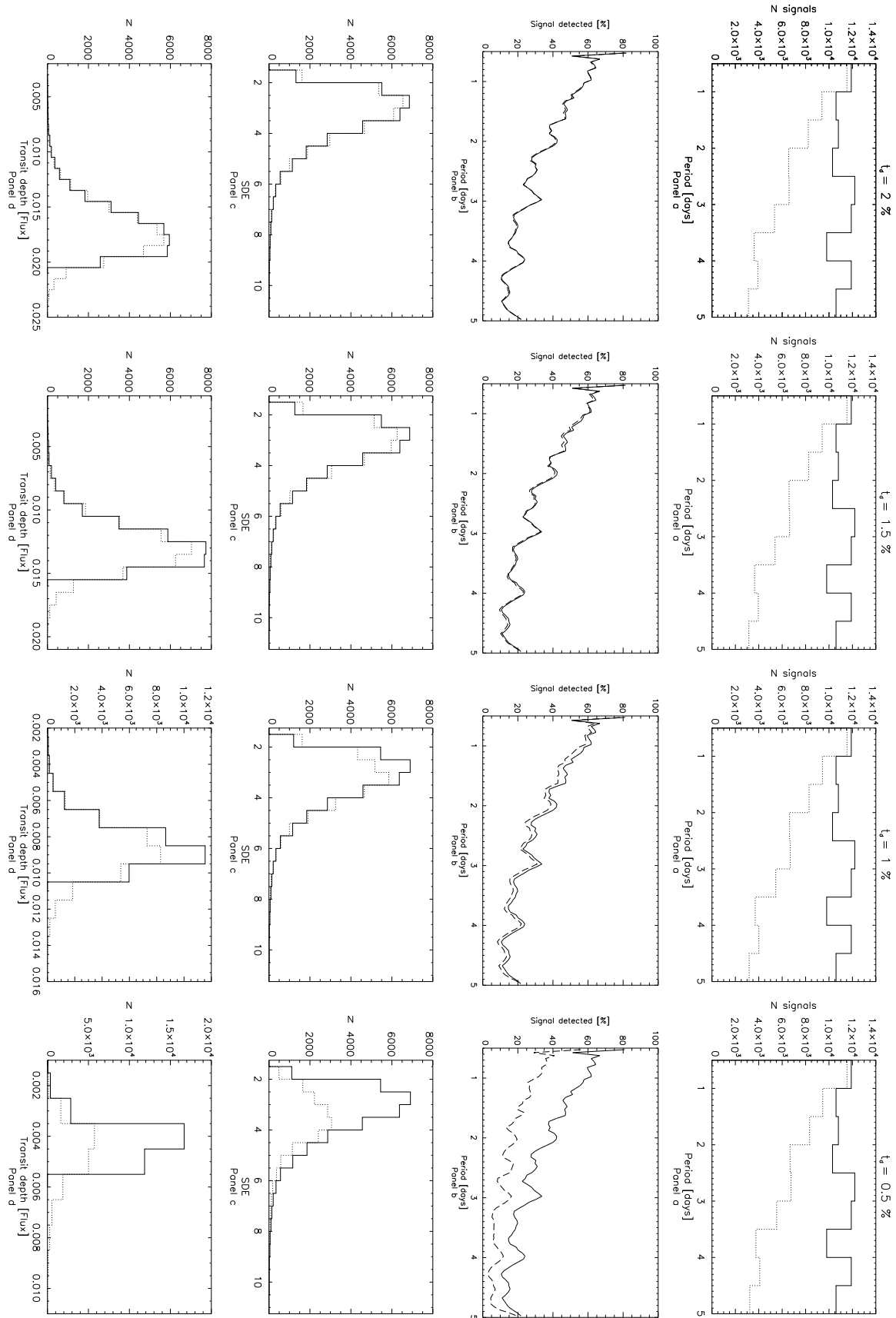


Figure 14. Summary of simulation output for LHS 417 (see text for details). Panels *a*: number of signals vs period; Panels *b*: detection probability vs period; Panels *c*: SDE distributions; Panels *d*: distributions of transit depths of the detected signals.

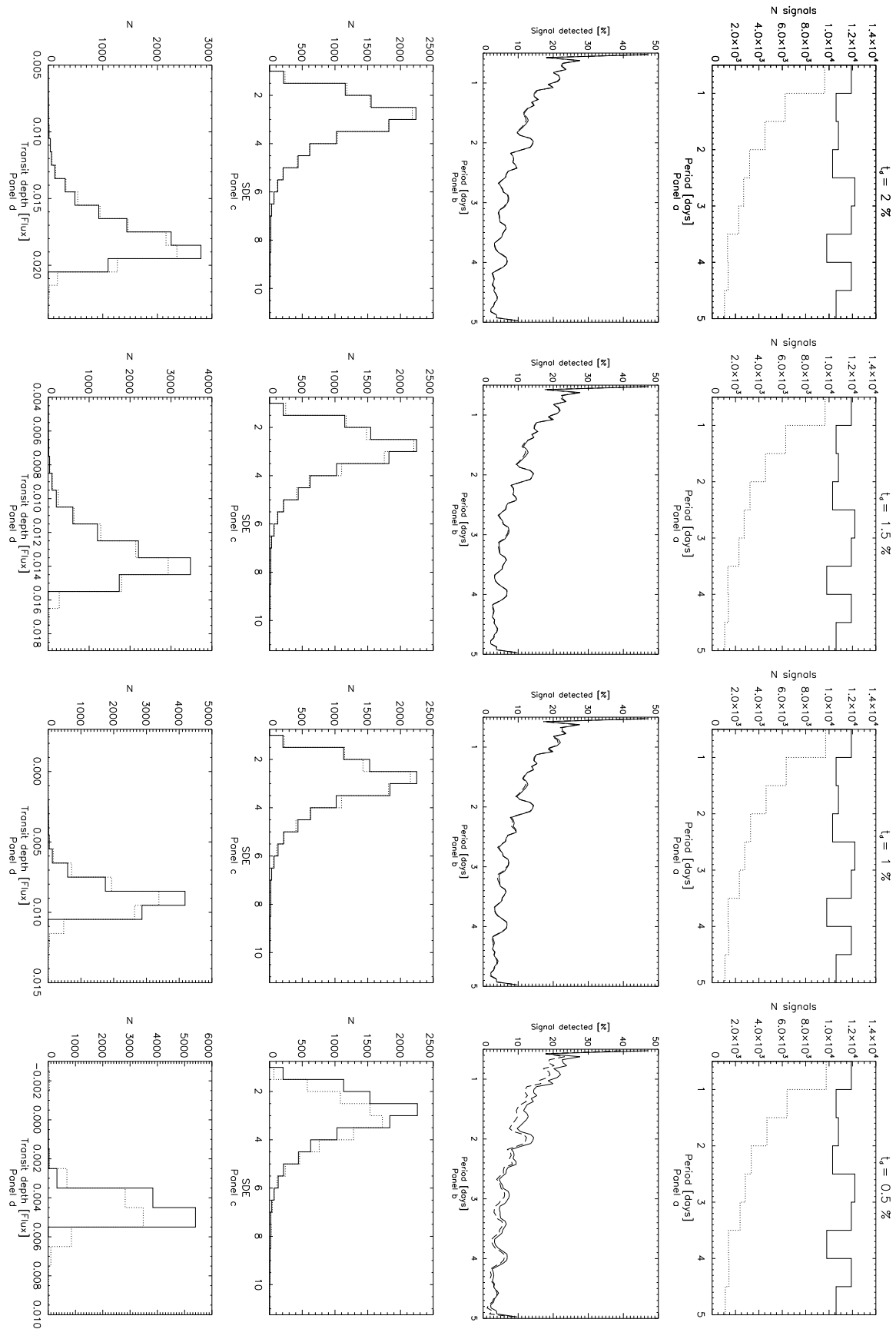


Figure 15. Summary of simulation output for LHS 3343 (see text for details). Panels *a*: number of signals vs period; Panels *b*: detection probability vs period; Panels *c*: SDE distributions; Panels *d*: distributions of transit depths of the detected signals.

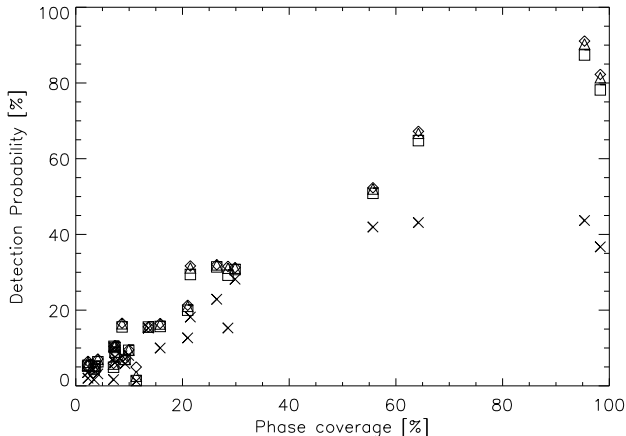


Figure 16. Average detection probability as a function of average phase coverage over the period range 0.5-5.0 days. Different symbols are used to show the trend of detection probability for the four regimes of transit depth simulated ($t_d = 2.0\%$: diamonds; $t_d = 1.5\%$: triangles; $t_d = 1.0\%$: squares; $t_d = 0.5\%$: crosses).

of bins to 300, and we recovered a transit depth in good agreement with the published one (nearly 2%).

The previous considerations allow us to relate directly the two comparison metrics whose properties we have analysed here, i.e. transit detection probability and phase coverage. We show in Figure 16, for the full stellar sample under investigation and using the simulation results based on light curves obtained with method *m3*, the detection probability as a function of the phase coverage, both averaged over the whole period range 0.5 – 5.0 days. Different symbols are used to show the trend of detection probability for the four regimes of transit depth simulated. For the definitions of transit detection probability and phase coverage provided above, the plot suggests a limit to the probability of detecting a transit, at least utilizing a real-life detection algorithm such as BLS, even when the phase coverage is almost 100%, a limit which becomes severe when the magnitude of the signal approaches the typical precision of the photometry. We believe that this effect is due to several factors, which include (but are not limited to): a) the way we actually define a detection: As discussed above, we adopt here a conservative definition, likely contributing to missing some of the correctly identified transit depths simply because the period did not fall within the stringent agreement constraints required; b) the fact that detection probabilities are averaged over period ranges which include values (close to integer and half-integer days) not optimally sampled in a ground-based, single-site campaign (see Figure 12); and c) the way we actually define the phase coverage: The choice of bin size and the prescription for the number of points in a bin required to define a specific phase covered can also impact the likelihood that the transit will be detected at that specific phase.

Similarly, Figure 17 shows the trend of detection probability as a function of phase coverage when limiting ourselves to the period range 0.5-1.0 days. Overall, for objects with good ($> 50\%$) phase coverage, we would have had $> 80\%$ chances of detecting transiting companions with transit depths in the range $0.5\% < t_d \leq 2\%$. Given the estimated stellar radii for these stars, this translates in a sensitivity to companions with minimum radii in the range $\sim 1.0 - 2.2 R_{\oplus}$. Figure 17 also shows how, when enough transits

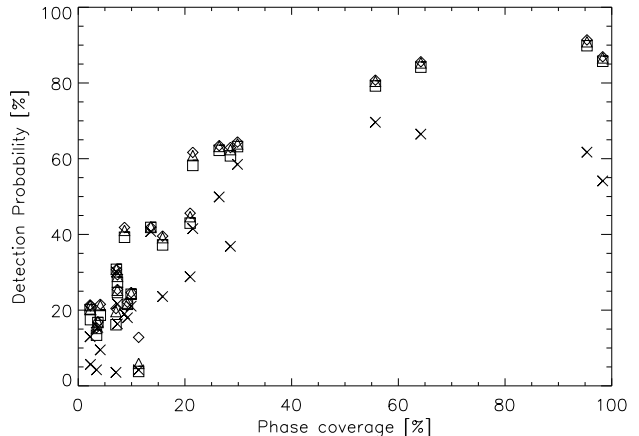


Figure 17. Average detection probability as a function of average phase coverage for $P < 1.0$ days. All symbols are as described in Figure 16.

($\gg 3$) are observed, even signals of magnitude comparable to the photometric precision can be reliably retrieved in our data.

As mentioned earlier, the results shown here cover the analysis of the simulation based on light curves derived with the *m3* photometric analysis method. The results based on the other three intra-night methods (not shown here) are very similar while they worsen significantly when the full-period light curves are considered. This is an expected result because those methods produce more noisy light curves (see § 4.1). However, such an effect is cause of no significant worries, as operationally transit-like events, whose duration for objects in short periods does not exceed the typical length of observations during one single night, are to be searched for in nightly-reduced differential photometric datasets.

To conclude, two points are worth mentioning further here. First, in a large-scale survey of thousands of *M* dwarfs, while some degree of prioritization of the targets based on their measured and/or inferred variability properties (based, e.g., on activity indicators and rotation information) will be possible, for many stars disregarding variability will simply not be an option. As for the two stars for which we successfully determined rotation periods, the probability of detection of a transit is not affected by the presence of the rotational modulation effect, as in both cases the time-scales of central transit events probed in our simulations (between 0.8 hr and 1.8 hr for LHS 3445 and between 0.4 hr and 0.9 hr for GJ 1167A) are significantly shorter than the observed rotational periods. Certainly, for much longer transit durations, or much shorter rotational periods, variability can instead become a matter of concern as it would directly interfere with a transit search. Rotational modulation on time-scales of 0.1 days is indeed observed (e.g., Irwin et al. 2011), and such issue will be addressed and dealt with in detail in the future. Second, variable degrees of correlated noise, either instrumental (tracking, flat-fielding), environmental (airmass, absorption, seeing) or astrophysical (colour, variability) in nature, can also affect our capability to detect transits. As shown by Pont et al. (2006), red noise primarily impacts the significance thresholds with which a transit event can be recovered from the data in a survey. As discussed in § 4.1.2, it constitutes a challenge to be able to fully characterize the relative role played by correlated noise sources on the potential of a photometric survey to detect statistically significant transit events, as this analysis will also depend on the details of the observed target populations. In the future, such an assessment

will be made using our survey data and a statistically significant sample of targets.

5 SUMMARY AND CONCLUSIONS

We report results of a one-year long photometric monitoring campaign of a sample of 23 nearby ($d < 60$ pc), bright ($J < 12$) M dwarfs carried out in Italy at the Astronomical Observatory of the Autonomous Region of the Aosta Valley (OAVdA), using small-size (< 1 -m class) telescopes. This survey was conceived as a necessary preparatory step towards a long-term search for transiting, small-radius planets around thousands of dM stars, which will be conducted at OAVdA with an array of automated 40-cm telescopes, beginning early 2012. This ‘pilot study’ was designed to achieve two goals: 1) demonstrate the sensitivity to $< 4 R_{\oplus}$ transiting planets with periods of a few days around our program stars, through a two-fold approach that combines a characterization of the statistical noise properties of our photometry with the determination of transit detection probabilities via simulations, and b) where possible, improve our knowledge of some astrophysical properties (e.g., activity, rotation) of our targets through a combination of spectroscopic information and our differential photometric measurements. At a technical level, the results we obtained during the pilot study are instrumental to the accurate design and fine tuning of several aspects of our upcoming photometric survey, such as the definition of the best observational strategy, the optimization of the target list, and the identification of improvements to be carried out on the pipeline for the photometric data reduction and time-series periodicity analysis. Our main findings can be summarized as follows:

- *Photometric precision.* We achieve a typical nightly RMS photometric precision of ~ 5 mmag, with little or no dependence on the instrumentation adopted or on the details of the methodology (different comparison stars selection criteria, use of different detrending algorithms) utilized to perform differential photometry on the targets. We also carried out an analysis of the impact of correlated (red) noise on time-scales of ~ 30 min, which showed that it is typically a factor ~ 1.3 greater than pure white noise, with a weak dependence on the method used to perform differential photometry. This result reveals that our data are only mildly affected by short-term correlated systematics. The estimated photometric precision degrades to ~ 9 mmag when the ensemble light curves are determined over the typical ~ 2 months duration of the observations for each target. Such degradation is understood in terms of a combination of unmodeled medium-term systematics in our data and intrinsic variability of our target stars.

- *Stellar variability analysis.* We searched for periodic transit-like events in the photometric dataset for each target using the BLS algorithm. No such signal was recovered for any target. This is an expected result given the sample size, thus meaningful constraints/upper limits on the planet fraction as a function of radius and orbital separation cannot be provided. The light curves of our program stars were inspected for evidence of periodic signals of approximately sinusoidal shape, which could be interpreted as due to the presence of rotating spots on the stellar photosphere. For two stars in our sample, LHS 3445 and GJ 1167A, we found clear evidence of a periodicity in the light curve ascribable to such effect. We determined photometric rotation periods of ~ 0.47 days and ~ 0.22 days for LHS 3445 and GJ 1167A, respectively; these estimates were confirmed by the large projected rotational velocities ($v \sin i \sim 25$ km/s and $v \sin i \sim 33$ km/s, respectively) inferred for both stars based on the analysis of archival high-resolution

Keck/HIRES spectra. The estimated inclinations of the stellar rotation axes for LHS 3445 and GJ 1167A agree with those derived using a simple spot model, which successfully reproduces the observed sinusoidal photometric variations in both cases (the dispersion of the post-fit residuals is on the order of the sample photometric precision). Finally, we detected short-term, low-amplitude flaring events in the differential photometric measurements of LHS 3445 and LHS 2686 (the latter not known to be a flare star). LHS 3445 was observed flaring three times, and two flares were recorded almost consecutively during the same night, with an approximately equal decay time of ~ 4.5 min, possibly a case of homologous flares.

- *Sensitivity to small-radius transiting planets.* We carried out large-scale simulations of transit signals (of periods in the range 0.5 – 5 days and depths in the range 0.5%-2% in flux units) injected in the actual (nightly reduced) photometric data for our sample. A total of 400,000 light curves were analysed for each target using a real-life transit events search algorithm (BLS). The study of the BLS transit recovery rates and overall performance for a sub-sample of stars with good, fair, and poor phase coverage highlighted the capability of BLS to identify the correct period (when multiple transits were observed) even for signals with depth close to the typical photometric precision of the data (~ 5 mmag), albeit with low statistical confidence, as well as some of its performance limitations which are driven by the specific choice of its most relevant setup parameters. We expressed our main findings in terms of two easy-to-use comparison metrics, i.e. transit detection probabilities and phase coverage. We found a quasi-linear relationship between the two quantities. Based on the BLS algorithm, there appears to be a limit of $\approx 90\%$ in the probability of detecting a transit even when the phase coverage approaches 100%. Around stars in our sample with good phase coverage ($> 50\%$), we would have had $> 80\%$ chances of detecting companions with $P < 1$ day and transit depths $> 0.5\%$ in flux units. Correspondingly, around these stars we would have been sensitive to companions with radii as small as $\sim 1.0 - 2.2 R_{\oplus}$.

The main findings reported here provide useful information for the purpose of the design and implementation of the operations of a ground-based M dwarf transit survey, with the aim of maximizing the chances for small-radius planet detection and improving our understanding of several astrophysically interesting properties of M dwarfs, particularly when investigated by means of statistical analyses of large stellar samples. Together with other similar efforts carried out by other groups, such as the pioneering MEarth program, the photometric database populated by our survey data will be of great help, for example, a) to improve the characterization of nearby M dwarf stars, when combined with Gaia’s exquisitely accurate astrometry (e.g., Sozzetti 2011), and b) to optimize the target selection criteria for red dwarfs which might be included in next-generation space-based transit survey programs, such as TESS (Ricker et al. 2010) and PLATO (Rauer & Catala 2011) or which might be selected for spectroscopic characterization of planetary atmospheres of transiting planets found orbiting cool, nearby stars with future space-borne infrared observatories such as EChO (Tinetti et al. 2011) and FINESSE (Swain 2010).

A forthcoming paper will present in detail all relevant aspects of the upcoming survey, including overall systems description, operations control software, target selection criteria, robust reduction pipeline and archiving.

ACKNOWLEDGMENTS

We warmly thank the anonymous referee for providing very useful comments and insightful suggestions which greatly helped to materially improve the paper. This research has made use of the SIMBAD database, operated at CDS, Strasbourg, France, and of the Keck Observatory Archive (KOA), which is operated by the W. M. Keck Observatory and the NASA Exoplanet Science Institute (NExSci), under contract with the National Aeronautics and Space Administration. MD, PC, AB, and GT are supported by grants of the European Union, the Autonomous Region of the Aosta Valley and the Italian Department for Work, Health and Pensions. The OAVdA is supported by the Regional Government of Valle d'Aosta, the Town Municipality of Nus and the Monte Emilius Community. We thank Davide Cenadelli (OAVdA) for his contribution in the analysis of the Keck/HIRES archival spectra.

REFERENCES

- Abell, P., Allison, J., Anderson, S. F., Andrew, J. R., Angel, J. R. P., Armus, L., Arnett, D., Asztalos, S. J., et al. 2009, *LSST Science Book* (arXiv:0912.0201)
- Adams, E. R., Seager, S., Elkins-Tanton, L. 2008, *ApJ*, 673, 1160
- Aerts, C., Christensen-Dalsgaard, J., and Kurtz, D. W., 2010, *Asteroseismology*, Springer Ed.
- Ambartsumyan, V. A., Mirzoyan, L. V., Parsamyan, E. S., Chavushyan, O. S., Erastova, L. K. 1970, *Astrofizika*, 6, 7
- Apps, K., Clubb, K. I., Fischer, D. A., Gaidos, E., Howard, A., Johnson, J. A., Marcy, G. W., Isaacson, H., et al. 2010, *PASP*, 122, 156
- Audard, M., Güdel, M., Drake, J. J., Kashyap, V. L. 2000, *ApJ*, 541, 396
- Bailer-Jones, C. A. L., Lamm, M. 2003, *MNRAS*, 339, 477
- Barnes, J.R., Jeffers, S.V., Jones, H.R.A. 2011, *MNRAS*, 412, 1599
- Bayless, A. J., & Orosz, J. A. 2006, *ApJ*, 651, 1155
- Bean, J. L., Sneden, C., Hauschildt, P. H., Johns-Krull, C. M., Benedict, G. F. 2006, *ApJ*, 652, 1604
- Bean, J. L., Miller-Ricci Kempton, E., Homeier, D. 2010, *Nature*, 468, 669
- Bean, J. L., Désert, J.-M., Kabath, P., Stalder, B., Seager, S., Miller-Ricci Kempton, E., Berta, Z. K., Homeier, D., et al. 2011, *ApJ*, 743, 92
- Beatty, T. G., et al. 2007, *ApJ*, 663, 573
- Bochanski, J. J., Hawley, S. L., Reid, I. N., Covey, K. R., West, A. A., Tinney, C. G., Gizis, J. E. 2005, *AJ*, 130, 1871
- Boisse, I., Bouchy, F., Hébrard, G., Bonfils, X., Santos, N., Vauclair, S. 2011, *A&A*, 528, A4
- Bonfils, X., Delfosse, X., Udry, S., Santos, N. C., Forveille, T., Ségransan, D. 2005, *A&A*, 442, 635
- Bonfils, X., Mayor, M., Delfosse, X., Forveille, T., Gillon, M., Perrier, C., Udry, S., Bouchy, F., et al. 2007, *A&A*, 474, 293
- Browning, M. K., Basri, G., Marcy, G. W., West, A. A., Zhang, J. 2010, *AJ*, 139, 504
- Burke, C. J., Gaudi, B. S., DePoy, D. L., Pogge, R. W. 2006, *AJ*, 132, 210
- Casagrande, L., Flynn, C., Bessell, M. 2008, *MNRAS*, 389, 585
- Charbonneau, D., Berta, Z. K., Irwin, J., Burke, C. J., Nutzman, P., Buchhave, L. A., Lovis, C., Bonfils, X., et al. 2009, *Nature*, 462, 891
- Ciardi, D. R., von Braun, K., Bryden, G., van Eyken, J., Howell, S. B., Kane, S. R., Plavchan, P., Ramírez, S. V., et al. 2011, *AJ*, 141, 108
- Claret, A. 2000, *A&A*, 363, 1081
- Croll, B., Albert, L., Jayawardhana, R., Miller-Ricci Kempton, E., Fortney, J. J., Murray, N., Neilson, H. 2011, *ApJ*, 736, 78
- Crossfield, I. J. M., Barman, T., Hansen, B. M. S. 2011, *ApJ*, 736, 132
- Damasso, M., Giacobbe, P., Calciolone, P., Sozzetti, A., Lattanzi, M. G., Bernagozzi, A., Bertolini, E., Smart, R. L. 2010, *PASP*, 122, 1077
- Deeming, T. J. 1975, *Ap&SS*, 36, 137
- Delfosse, X., Forveille, T., Ségransan, D., Beuzit, J.-L., Udry, S., Perrier, C., Mayor, M. 2000, *A&A*, 364, 217
- Désert, J.-M., Bean, J., Miller-Ricci Kempton, E., Berta, Z. K., Charbonneau, D., Irwin, J., Fortney, J., Burke, C. J., et al. 2011, *ApJ*, 731, L40
- Doyle, J. G., Butler, C. J., van den Oord, G. H. J., Kiang, T. 1990, *A&A*, 232, 93
- Droege, T. F., Richmond, M. W., Sallman, M. 2006, *PASP*, 118, 1666
- Dumusque, X., Santos, N. C., Udry, S., Lovis, C., Bonfils, X. 2011, *A&A*, 527, A82
- Eggenberger, A., Udry, S. 2010, *EAS Pub. Ser.*, 41, 27
- Endl, M., Cochran, W. D., Kürster, M., Paulson, D. B., Wittenmyer, R. A., MacQueen, P. J., Tull, R. G. 2006, *ApJ*, 649, 436
- Ferraz-Mello, S., Tadeu Dos Santos, M., Beaugé, C., Michtchenko, T. A., Rodríguez, A. 2011, *A&A*, 531, A161
- Fischer, D. A., Valenti, J. 2005, *ApJ*, 622, 1102
- Forveille, T., Bonfils, X., Lo Curto, G., Delfosse, X., Udry, S., Bouchy, F., Lovis, C., Mayor, M., et al. 2011, *A&A*, 526, A141
- Gershberg, R.E., Katsova, M.M., Lovkaya, M.N., Terebizh, A.V., Shakhovskaya, N.I. 1999, *A&AS*, 139, 555
- Gizis, J. E., Reid, I. N., Hawley, S. L. 2002, *AJ*, 123, 3356
- Gregory, P. C. 2011, *MNRAS*, 415, 2523
- Güdel, M., Audard, M., Kashyap, V. L., Drake, J. J., Guinan, E. F. 2003, *ApJ*, 582, 423
- Gustafsson, B. 1989, *ARA&A*, 27, 701
- Guinan, E. F., Engle, S. G., Mizusawa, T., McCook, G. P., Wolfe, A., Coughlin, J. 2009, *Highlights of Astronomy*, 15, 703
- Gray, D. F. 2008, *The Observation and Analysis of Stellar Photospheres*, by D. F. Gray. Cambridge: Cambridge University Press, 2008
- Haghighipour, N., Vogt, S. S., Butler, R. P., Rivera, E. J., Laughlin, G., Meschiari, S., Henry, G. W. 2010, *ApJ*, 715, 271
- Hartman, J. D., Gaudi, B. S., Pinsonneault, M. H., Stanek, K. Z., Holman, M. J., McLeod, B. A., Meibom, S., Barranco, J. A., et al. 2009, *ApJ*, 691, 342
- Hartman, J.D., Bakos, G.Á., Noyes, R.W., Sipocz, B., Kovács, G., Mazeh, T., Shporer, A., Pál, A. 2011, *AJ*, 141, A166
- Hatzes, A. P., Dvorak, R., Wuchterl, G., Guterman, P., Hartmann, M., Fridlund, M., Gandolfi, D., Guenther, E., et al. 2010, *A&A*, 520, A93
- Henry, T. J., Jao, W., Subasavage, J. P., Beaulieu, T. D., Ianna, P. A., Costa, E., Mndez, R. A. 2006, *AJ*, 132, 2360
- Howard, A.W., Marcy, G.W., Bryson, S.T., Jenkins, J.M., Rowe, J.F., Batalha, N.M., Borucki, W.J., Koch, D.G., et al. 2011, *ApJ* submitted (arXiv:1103.2541)
- Ida, S., Lin, D. N. C. 2004, *ApJ*, 616, 567
- Ida, S., Lin, D. N. C. 2005, *ApJ*, 626, 1045
- Irwin, J., Irwin, M., Aigrain, S., Hodgkin, S., Hebb, L., Moraux, E. 2007, *MNRAS*, 375, 1449
- Irwin, J., Berta, Z. K., Burke, C. J., Charbonneau, D., Nutzman,

- P., West, A. A., Falco, E. E. 2011, *ApJ*, 727, 56
- Jenkins, J. S., Ramsey, L. W., Jones, H. R. A., Pavlenko, Y., Gallardo, J., Barnes, J. R., Pinfield, D. J. 2009, *ApJ*, 704, 975
- Johnson, J. A., Fischer, D. A., Marcy, G. W., Wright, J. T., Driscoll, P., Butler, R. P., Hekker, S., Reffert, S., et al. 2007, *ApJ*, 665, 785
- Johnson, J. A., Apps, K. 2009, *ApJ*, 699, 933
- Johnson, J. A., Aller, K. M., Howard, A. W., Crepp, J. R. 2010, *PASP*, 122, 905
- Johnson, J. A., Clanton, C., Howard, A. W., Bowler, B. P., Henry, G. W., Marcy, G. W., Crepp, J. R., Endl, M., et al. 2011a, *ApJS*, 197, 26
- Johnson, J. A., Gazak, J. Z., Apps, K., Muirhead, P. S., Crepp, J. R., Crossfield, I. J. M., Boyajian, T., von Braun, K., et al. 2012, *AJ*, 143, 111
- Lenz, P., & Breger, M. 2005, *Communications in Asteroseismology*, 146, 53
- Kaiser, N. 2004, in *Ground-based Telescopes. Proc. SPIE*, 5489, 11
- Kasting, J. F., Whitmire, D. P., & Reynolds, R. T. 1993, *Icarus*, 101, 108
- Kennedy, G. M., Kenyon, S. J. 2008, *ApJ*, 682, 1264
- Kharchenko, N. V., 2001, *Kinematika Fiz. Nebesn. Tel.*, 17, 409
- Kovács, G., Zucker, S., & Mazeh, T. 2002, *A&A*, 391, 369-377
- Kovács, G., Bakos, G., Noyes, R. W. 2005, *MNRAS*, 356, 557
- Kowalski, A. F., Hawley, S. L., Hilton, E. J., Becker, A. C., West, A. A., Bochanski, J. J., Sesar, B. 2009, *AJ*, 138, 633
- Krautter, J. 1996, in *Light Curves of Variable Stars: a Pictorial Atlas*, ed. C. Jaschek & C. Sterken (Cambridge: Cambridge Univ. Press), 53
- Lacy, C. H., Moffett, T. J., & Evans, D. S. 1976, *ApJS*, 30, 85
- Lagrange, A.-M., Desort, M., Meunier, N. 2010, *A&A*, 512, A38
- Lammer, H., Lichtenegger, H. I. M., Kulikov, Y. N., Griemeier, J.-M., Terada, N., Erkaev, N. V., Biernat, H. K., Khodachenko, M. L., et al. 2007, *Astrobiology*, 7, 185
- Laughlin, G., Bodenheimer, P., Adams, F. C. 2004, *ApJ*, 612, L73
- Law, N. M., Kulkarni, S. R., Dekany, R. G., Ofek, E. O., Quimby, R. M., Nugent, P. E., Surace, J., Grillmair, C. C., et al. 2009, *PASP*, 121, 1395
- Lépine, S. & Shara, P. 2005, *AJ*, 129, 1438
- Lépine, S. 2005, *AJ*, 130, 1680
- Levenberg, K. 1944, *Quart. Appl. Math.*, 2, 164
- López-Morales, M. 2007, *ApJ*, Vol. 660, Issue 1, pp. 732-739
- López-Santiago, J., Montes, D., Gálvez-Ortiz, M. C., Crespo-Chacón, I., Martínez-Arnáiz, R. M., Fernández-Figueroa, M. J., de Castro, E., Cornide, M. 2010, *A&A*, 514, A97
- Mandel, K. & Agol, E. 2002, *ApJ*, 580, L171
- Makarov, V. V., Beichman, C. A., Catanzarite, J. H., Fischer, D. A., Lebreton, J., Malbet, F., Shao, M., 2009, *ApJ*, 707, L73
- Markwardt, C. B. 2009, *arXiv:0902.2850*
- Marquardt, D. 1963, *SIAM J. Appl. Math.*, 11, 431
- Martres, M.-J., Mein, N., Mouradian, Z., Rayrole, J., Schmieder, B., Simon, G., Soru-Escout, I., Woodgate, B. E. 1984, *AdSR*, 4, 5
- Meibom, S., Mathieu, R. D., Stassun, K. G. 2009, *ApJ*, 695, 679
- Miller-Ricci, E., & Fortney, J. J. 2010, *ApJ*, 716, L74
- Miller-Ricci Kempton, E., Zahnle, K., Fortney, J. J. 2011, *ApJ*, 745, 3
- Mirzoyan, L. V., Ambaryan, V. V., Garibdzhanyan, A. T., Mirzoyan, A. L. 1989, *Astrophysics*, 31, 567
- Moffett, T. J. 1974, *ApJS*, 29, 1
- Mordasini, C., Alibert, Y., Benz, W., Naef, D. 2009, *A&A*, 501, 1161
- Nettelmann, N., Fortney, J. J., Kramm, U., Redmer, R. 2011, *ApJ*, 733, 2
- Nutzman, P., & Charbonneau, D. 2008, *PASP*, 120, 317
- Pepe, F., Mayor, M., Lovis, C., Benz, W., Bouchy, F., Dumusque, X., Queloz, D., Santos, N. C., et al. 2011, *Proc. IAU Symp.* 276, 13
- Phan-Bao, N., Lim, J., Donati, J.-F., Johns-Krull, C. M., Martín, E. L. 2009, *ApJ*, 704, 1721
- Pizzolato, N., Maggio, A., Micela, G., Sciortino, S., Ventura, P. 2003, *A&A*, 397, 147
- Pont, F., Zucker, S., Queloz, D. 2006, *MNRAS*, 373, 231
- Pont, F., Aigrain, S., Zucker, S. 2011, *MNRAS*, 411, 1953
- Queloz, D., Henry, G. W., Sivan, J. P., Baliunas, S. L., Beuzit, J. L., Donahue, R. A., Mayor, M., Naef, D., et al. 2001, *A&A*, 379, 279
- Queloz, D., Bouchy, F., Moutou, C., Hatzes, A., Hébrard, G., Alonso, R., Auvergne, M., Baglin, A., et al. 2009, *A&A*, 506, 303
- Ranns, N. D. R., Harra, L. K., Matthews, S. A., Culhane, J. L. 2000, *A&A*, 360, 1163
- Rauer, H., & Catala, C. 2011, *Proc. IAU Symp.* 276, 354
- Reid, I. N., Mahoney, S. 2000, *MNRAS*, 316, 827
- Reid I.N., Cruz K.L. 2002, *Astron. J.* 123, 2006
- Reiners, A. 2007, *A&A*, 467, 259
- Reiners, A., Basri, G. 2010, *A&A*, 710, 924
- Reiners, A., Bean, J. L., Huber, K. F., Dreizler, S., Seifahrt, A., Czesla, S. 2010, 710, 432
- Ribas, I. 2006, *Ap&SS*, 304, 89
- Ricker, G. R., Latham, D. W., Vanderspek, R. K., Ennico, K. A., Bakos, G., Brown, T. M., Burgasser, A. J., Charbonneau, D., et al. 2010, *BAAS*, 42, 459
- Rojas-Ayala, B., Covey, K. R., Muirhead, P. S., Lloyd, J. P. 2010, *ApJ*, 720, L113
- Rogers, L. A., Seager, S. 2010, *ApJ*, 716, 1208
- Santos, N. C., Israelian, G., Mayor, M. 2004, *A&A*, 415, 1153
- Scalo, J., Kaltenegger, L., Segura, A. G., Fridlund, M., Ribas, I., Kulikov, Yu.N., Grenfell, J.L., Rauer, H., et al. 2007, *Astrobiology*, 7, 85
- Schlaufman, K. C., Laughlin, G. 2010, *A&A*, 519, A105
- Seager, S. & Mallen-Ornelas, G. 2003, *ApJ*, 585, 1038
- Seager, S., Deming, D. 2010, *ARA&A*, 48, 631
- Shkolnik, E., Liu, M. C., Reid, I. N. 2009, *ApJ*, 699, 649
- Smart, R. L., Ioannidis, G., Jones, H. R. A., Bucciarelli, B., & Lattanzi, M. G. 2010, *A&A*, 514, A84
- Sozzetti, A., Torres, G., Latham, D. W., Stefanik, R. P., Korzennik, S. G., Boss, A. P., Carney, B. W., Laird, J. B. 2009, *ApJ*, 697, 544
- Sozzetti, A. 2011, *EAS Pub. Ser.*, 45, 273
- Stellingwerf, R. F. 1978, *ApJ*, 224, 953
- Strassmeier, K., Washuettl, A., Granzer, Th., Scheck, M., Weber, M. 2000, *A&AS*, 142, 275
- Swain, M. R. 2010, *BAAS*, 42, 1064
- Tamuz, O., Mazeh, T., Zucker, S. 2005, *MNRAS*, 256, 1466
- Tarter, J.C., Backus, P.R., Mancinelli, R.L., Aurnou, J.M., Backman, D.E., Basri, G.S., Boss, A.P., Clarke, A., et al. 2007, *Astrobiology*, 7, 30
- Tinetti, G., Beaulieu, J.P., Henning, T., Meyer, M., Micela, G., Ribas, I., Stam, D., Swain, M., et al. 2011, *Exp. Ast.*, accepted (arXiv:1112.2728)
- Torres, G., Andersen, J., Giménez, A. 2010, *A&ARv*, 18, 67
- Tuomi, M. 2011, *A&A*, 528, L5
- Van Leeuwen, F. 2007, *A&A*, 474, 653

- Vogt, S. S., Butler, R. P., Rivera, E. J., Haghighipour, N., Henry, G. W., Williamson, M. H. 2010, ApJ, 723, 954
- Walkowicz, L. M., & Hawley, S.L. 2009, AJ, 137, 3297
- West, A. A., Basri, G. 2009, ApJ, 693, 1283
- West, A. A., Bochanski, J. J., Bowler, B. P., Dotter, A., Johnson, J. A., Lépine, S., Rojas-Ayala, B., Schweitzeret A. 2011, ASP. Conf. Ser., 448, 531
- Woolf, V. M., Wallerstein, G. 2006, PASP, 118, 218
- Woolf, V. M., Lépine, S., Wallerstein, G. 2009, PASP, 121, 117
- Wright, J. T., Marcy, G. W., Butler, R. P., Vogt, S. S. 2004, ApJS, 152, 261
- Zechmeister, M., Kürster, M., Endl, M. 2009, A&A, 505, 859
- Zucker, S., & Mazeh, T. 1994, ApJ, 420, 806